INFORMATION TO USERS

This manuscript has been reproduced from the microfilm master. UMI films the text directly from the original or copy submitted. Thus, some thesis and dissertation copies are in typewriter face, while others may be from any type of computer printer.

The quality of this reproduction is dependent upon the quality of the copy submitted. Broken or indistinct print, colored or poor quality illustrations and photographs, print bleedthrough, substandard margins, and improper alignment can adversely affect reproduction.

In the unlikely event that the author did not send UMI a complete manuscript and there are missing pages, these will be noted. Also, if unauthorized copyright material had to be removed, a note will indicate the deletion.

Oversize materials (e.g., maps, drawings, charts) are reproduced by sectioning the original, beginning at the upper left-hand corner and continuing from left to right in equal sections with small overlaps. Each original is also photographed in one exposure and is included in reduced form at the back of the book.

Photographs included in the original manuscript have been reproduced xerographically in this copy. Higher quality 6" x 9" black and white photographic prints are available for any photographs or illustrations appearing in this copy for an additional charge. Contact UMI directly to order.

U·M·I

University Microfilms International
A Bell & Howell Information Company
300 North Zeeb Road, Ann Arbor, MI 48106-1346 USA
313/761-4700 800/521-0600

Order Number 9325079

Magnetic anisotropies in SmCo thin films

Chen, Kailai, Ph.D.

City University of New York, 1993

U·M·I
300 N. Zeeb Rd.
Ann Arbor, MI 48106

MAGNETIC ANISOTROPIES IN SmCo THIN FILMS

by

KAILAI CHEN

A dissertation submitted to the Graduate Faculty in Physics in partial fulfillment of the requirements for the degree of Doctor of Philosophy, The City University of New York.

1993

This Manuscript has been read and accepted for the Graduate Faculty in Physics in satisfaction of the dissertation requirement for the degree of Doctor of Philosophy.

April 9, 1993
Date

Fred J. Cadieu
Chair of Examining Committee

April 13, 1993
Date

Joseph B Thaler
Executive Officer

Prof. Fred J. Cadieu

Prof. Rutherford C. Fischer

Prof. Alexander A. Lisyansky

Prof. Ying-Chih Chen

Dr. Ernest Potenziani II

Supervisory Committee

THE CITY UNIVERSITY OF NEW YORK

ACKNOWLEDGMENTS

I am grateful to my supervisor, Professor Fred J. Cadieu, for his continuous support and encouragement throughout this work. Without his generous support and assistance this thesis work would have been impossible. Special thanks to Research Associate Dr. Hari Hegde for his friendly help throughout the period of this research and the time he spent in reviewing this thesis. I am thankful to my fellow researchers Mr. Anil Navarathna, Ms. Raj Rani and Mr. P. Pubudu.

I would like to thank Professor Rutherford Fischer, Professor Alex Lisyansky, Professor Ying-Chih Chen and Dr. Ernie Potenziani for having served in my thesis Supervisory Committee.

I take this opportunity to thank my wife Wei for her continuous moral support and for bearing with me throughout the period of this research.

It is my pleasure to extend my sincere thanks to all members of the faculty and staff, colleagues, and friends at the Department of Physics, Queens College.

My thesis is part of the research program, studying the magnetic properties of rare-earth transition-metal permanent magnet system, principally supported by grants to Professor Cadieu from RADC/EEAC, Hanscom Air Force Base.

TABLE OF CONTENTS

List of Tables

List of Figures

CHAPTER 1 INTRODUCTION

In addition to their interest from the viewpoint of fundamental physics, thin film magnets have attracted much attention because of their potential application in storage media, small scale electromechanical devices, microwave devices, small scale integrated circuits and small film-scale permanent magnet geometries.(1)(2) Film permanent magnet field sources need no power supplies and provide great portability. Applications for thin film magnets can be found anywhere DC magnetic fields are required such as monolithic microwave integrated circuits or recording heads.

The intrinsic requirements for permanent magnet are high level of saturation magnetization, $4\pi Ms$, and strong uniaxial magnetocrystalline anisotropy field, H_k. Since most permanent magnetic materials are used in the form of fine particle magnets, it is also important to assemble the fine particles in such a way that their easy magnetization directions are well aligned.

In the case of film permanent magnets, the same requirements still apply. Thus the fabrication of film magnets consists of obtaining high energy product magnetic materials in film form, and achieving high level of anisotropy properties in the film.

Films with various magnetic anisotropies can be synthesized through sputter deposition in both crystalline and amorphous phases. A systematic study of the deposition processes and magnetic properties for samarium-cobalt (Sm-Co) film system has been carried out in this work. Films of Sm-Co system with various magnetic anisotropies have been

synthesized through sputter deposition in both crystalline and amorphous phases. Their anisotropies have been characterized and sources of these anisotropies studied.

The highest energy product is achieved in rare-earth-transition-metal(RE-TM) materials. Among them, the Sm-Co based alloys and $Nd_2Fe_{14}B$ materials are the most important classes of permanent magnet materials with excellent intrinsic properties[3][4]. The Sm-Co based system is more favorable for film application because of its excellent high temperature stability. In this thesis, Sm-Co based material is chosen as the preferred material for synthesizing the film magnets.

The extensive research work on Sm-Co bulk magnets resulted in several metallurgical methods for the fabrication of $CaCu_5$ and Th_2Zn_{17} type magnets having energy products near 30MGOe.[3] The fabrication procedures usually include high temperature sintering of aligned, alloy powder compacts followed by thermal treatments. The high temperature (around 1000°C) thermal processing is necessary for optimizing the magnetic behavior of the magnets.

Differing from the fabrication of the bulk magnets, the synthesis of film magnets faces the difficulty of aligning the crystallites with nonrandom distributions of their easy magnetic axes in one step and eliminating the need for any high temperature thermal treatments.

The properties of thin films depend on the conditions at the substrate when the deposition atoms arrive. Major processing variables that may be used to modify the film properties include substrate temperature, kinetic energy of the deposition atoms, and deposition rate. These conditions determine the mobility of atoms on the film surface and thus the microstructure of the films. The crystal structure and texture of the films are also strongly affected by these conditions.

A sputter deposition method had been developed in our lab that allowed the synthesis of Sm-Co type film magnets that exhibit an in plane energy product in the 20MGOe range[5][6][7]. The films were of $TbCu_7$ type structure which is the disordered form of Th_2Zn_{17} type structure. The crystallites of these films had their c-axes aligned in the film plane. The films were synthesized in one step through the deposition of the Sm-Co materials onto heated substrate under properly chosen sputtering conditions without any post deposition thermal treatment. Thermallized sputtering was used in which the sputtering was carried out at a relatively high sputtering gas pressure so that the kinetic energy of deposition atoms is greatly reduced as they arrive at the substrate. It was found that the increased sputter gas pressure was crucial to obtain the textured films[7]. Similar methods have also allowed the synthesis of highly textured $ThMn_{12}$ type Sm-Fe-T films[8][9].

In this work, sputter deposition process control similar to that mentioned above was used to synthesize Sm-Co based films with rhombohedral 2-17 Th_2Zn_{17} type structure[10]. The Th_2Zn_{17} structure is a superstructure of $CaCu_5$ structure resulting from ordered substitution of one RE atom with a pair of TM atoms for every three unit cells of the $CaCu_5$ structure. However, when this substitution is partial, the substitutions are random, and the disordered $TbCu_7$ structure results. The Sm-Co based Th_2Zn_{17} type films have been synthesized with enriched Fe concentrations. The rhombohedral 2-17 grains exhibited unusually strong textures with their crystallographic c axis in the film plane. On Fe enrichment, due to the limited solubility of Fe in $CaCu_5$ structure, ordered Th_2Zn_{17} structure is formed. However, at similar deposition conditions and Sm concentrations, films with lower Fe formed in the $TbCu_7$ type disordered structure.

It is very important to understand the film growth processes in order to understand the formation of the magnetic anisotropy in the films. Magnetic anisotropy can occur during the sputter deposition process or as a result of post deposition heat treatment process. Both processes can lead to structures with nonrandom distributions of crystallographic orientations. Differing from epitaxial processes, the texture of sputter synthesized films in this work was build up during the deposition process without any initial texture. Thus the texture of the films is strongly dependent on the sputter process parameters (5) (7). A set of films with thickness from 500 Å to 2 micrometer were synthesized to investigate the early stage of the grain growth and the corresponding magnetic properties.

Although the above crystalline films have been synthesized with their easy axis in the film plane, their magnetic properties are nearly isotropic within the film plane. In-the-film-plane anisotropy can be induced in the SmCo films by applying a magnetic field in the film plane during deposition when the deposition temperature is below the crystallization temperature(11)(12)(13). Several models such as atomic pair ordering model, microcrystallite models and local structure models have been proposed to explain the origin of this anisotropy (11)(14)(15). But large discrepancies exist among various experimental results and the origin of the anisotropy built in by the growth process is far from well understood. In an attempt to better understand the formation and the origin of the anisotropy in amorphous-rare-earth transition-metal (a-RE-TM) films, the variation of in-the-film-plane anisotropy with composition and the magnitude of the field applied during the deposition has been studied. The dependence of anisotropy in amorphous SmCo films upon the process conditions, such as substrate temperature, sputtering rate and sputtering gas pressure, were also studied. It is concluded that surface induced short range ordering is the origin of the anisotropy observed in amorphous films deposited in the presence of a magnetic field and the formation mechanism is different from that of the short range ordering induced by field annealing(16).

It was found that both in-the-film-plane, and perpendicular, anisotropy could be present in sputter synthesized amorphous SmCo films depending on the film preparation conditions[17]. Different sources of anisotropy were distinguished in these films. The physical origin of in-the-film-plane anisotropy was explained as directional pair ordering. The perpendicular anisotropy was only formed in films synthesized through thermalized sputtering and can not be explained by directional pair ordering. A large anisotropy was observed in films deposited at above ambient temperatures, with easy axis in the film plane but without any preferred direction within the film plane. Both the formation of growth induced structure which caused the perpendicular anisotropy, and the formation of a third type of anisotropy, prevented the formation of pair ordering, and decreased in-the-film-plane anisotropy.

Finally, multilayered films have been sputter synthesized through modulation of the film growth[18]. In these modulated multilayer films, alternating layers were synthesized by modulation in terms of composition and texture.

The multilayered permanent magnet films were synthesized from TDK 2-17 type bulk targets. They comprised of alternating layers that exhibit relatively low and high coercivity respectively. This layered system was saturated in the film plane by applying a field in the film plane. The applied field then was reversed and raised to a level that only the moments in the lower coercivity layers were reversed. After the external field was removed, the in plane magnetization was oppositely directed in successive layers. To retain the high energy product for each layer in this state, besides having a large difference of coercivity between alternating layers, it was necessary for each layer to be synthesized with c-axes aligned in the film plane, so each layer has a square shaped hysteresis loop.

The alternating layer films were synthesized through sputter process control and method of crystallization. The layers with higher coercivity were subsequently crystallized after room temperature deposition in amorphous form while the lower coercivity layers were directly crystallized through deposition on a properly heated substrate. Since the temperature at which these films were deposited was much lower than the liquidus temperature, the diffusion between alternating layers was not significant. For the films with individual layer thickness around a micron, the magnetic properties of each layer was retained as in an isolated film. The differences in magnetic properties of successive layers became indistinguishable in the net hysteresis loop when the individual layer thickness was less than 500 Å.

The rest of the thesis is organized in the following way. In chapter 2, basic theoretical aspects are reviewed. It includes the fundamental considerations in the permanent magnetic materials, crystal structure of Sm-Co based alloys and the basic theory of the magnetic anisotropy. The experimental details are presented in chapter 3. Chapter 4 discusses the synthesis of Sm-Co based films with rhombohedral 2-17 Th_2Zn_{17} type structure. In-the-film-plane anisotropies are discussed in detail in chapter 5. Chapter 6 presents the results of the magnetic measurements for thin films with various thickness. The synthesis of modulated multilayer films are presented in chapter 7. chapter 8 contains concluding remarks.

CHAPTER 2 REVIEW OF THEORETICAL ASPECTS

2.1. Hysteresis Behavior

An external field changes the state of magnetization of a ferromagnetic material in a way that is nonlinear and irreversible. The hysteresis loop M(H) is traced reproducibly provided the applied field is sufficiently high to achieve saturation in each direction. The principal parameters used for characterizing permanent magnets are saturation magnetization $4\pi M_S$, remnant magnetization $4\pi M_r$, intrinsic coercivity iHc and maximum energy product $(BH)_{max}$ [19]. The saturation magnetization $4\pi M_S$ is an intrinsic property of the ferromagnetic phase, but the remanence $4\pi M_r$ and coercivity ${}_iH_c$ are not. $4\pi M_r$ and ${}_iH_c$ depend in a complex way on the particle size, shape and metallurgical microstructure of the magnet. The measure of quality for permanent magnets is the energy product $(BH)_{max}$ which is the maximum product of magnetic induction B and internal magnetic field H in the second quadrant of the B(H) hysteresis loop. $(BH)_{max}$ provides a measure of the field that can be produced outside a unit volume of magnet

materials. The theoretically maximum achievable value of the energy product for a particular material is $(4\pi M_s)^2/4$. For the case where the induction plot is characterized by a straight line in the second quadrant and the coercivity is large enough, the energy product is approximately $(4\pi M_r)^2/4$. In practice, the $4\pi M_r$ value is lower than $4\pi M_s$ because of poor particle alignment, less than theoretical density of the magnet, and second phases in the microstructure.

The internal field is given by $H_{int} = H_{appl} - N_dM$ where H_{appl} is the applied field, N_dM is the demagnetizing field, and N_d is the self-demagnetization factor. N_d depends mainly on the shape of the magnet and can be calculated exactly only for an ellipsoid[19]. Thin film can be approximately treated as a special case of ellipsoid, oblate spheroid. The normal sample size for magnetometer measurements is 4 mm by 4 mm in this study. Then the demagnetization factor for film with thickness t is[1] $N_{d\text{-}in} \approx (1/2)(t/2\text{ mm})4\pi$ for measurements in the film plane, and $N_{d\text{-}out} \approx 4\pi(1\text{-}t/2m)$ for measurements perpendicular to film plane. These relations are consistent with $N_{d\text{-}out} + 2N_{d\text{-}in} = 4\pi$.

The thicknesses of the films in this study is normally around 1 μm. Then we have $N_{d\text{-}out} \approx 4\pi(0.9995)$ and $N_{d\text{-}in} \approx 3\text{x}10^{-3}$. It is a good approximation that for measurements made parallel to the film plane, $N_d = 0$ and for measurments made perpendicular to film plane, $N_d = 4\pi$. Thus there is a large demagnetizing field present in the direction perpendicular to the film plane.

Large uniaxial anisotropy fields permit the attainment of high intrinsic coercivity ¡H_c. The anisotropy manifests itself as preferred directions in the material along which the moments align themselves. When an external magnetic field is applied along the preferred direction (easy axis), the material saturates easily compared to when the field direction is normal to it (hard axis). The anisotropy energy E can be expressed in terms of a series expansion of

the direction cosines of M_S relative to the axis. For uniaxial anisotropy, the anisotropy energy is expressed as $E_a=K_1\sin^2\phi + K_2\sin^4\phi + \ldots$, where the ϕ is the angle between the easy axes and the internal magnetization and K_1, K_2 are anisotropy constant.

The anisotropy can be obtained through torque curves, magnetization curves, or magnetic resonance.

Various anisotropies are classified as following(20):

(1) Magnetocrystalline anisotropy which is due mainly to spin-orbit coupling.

(2) Shape anisotropy which come from the demagnetization fields.

(3) Stress anisotropy which is produced by a combination of strain and magnetostriction in the crystal.

(4) Induced anisotropy which is due to an asymmetrical distribution of like or unlike atom pairs in the compound.

The physical origin of the anisotropy can also be grouped in the following categories:

(1) Anisotropy involving spin-orbit coupling. It can be either single-ion anisotropy in which aspherical charge distribution of non-S-state ions interact with crystalline field, or anisotropic exchange, in which magnetic ions interact with one another because of wave-function overlap; various terms in the interaction are called pseudodipolar and pseudoquadrupolar.

(2) Anisotropy involving magnetic dipolar interaction with contributions originating from microscopic atomic moment pairs which are not isotropically distributed.

(3) Anisotropy involving magnetostriction and anisotropic stress distributions.

2.2 Crystal Structure of SmCo Alloys.

The crystal structure data for the entire range of SmCo intermetallic compounds is given in Table 2.1. Among them, the $SmCo_5$ and rhombohedral Sm_2Co_{17} are the most important compounds as permanent magnets[3].

Figure 2.1 shows the crystal structure of the $SmCo_5$ phase. The $SmCo_5$ compound has hexagonal $CaCu_5$ structure and belongs to space group P6/mmm [21]. There is one site for the Sm atom and two for Co. The sites are listed as follows:

One Sm in site (a):
(0, 0, 0)
Two Co in site (c):
(2/3, 1/3, 0), (1/3, 2/3, 0)
Three Co in site (g):
(1/2, 1/2, 1/2), (1/2, 0, 1/2), (0, 1/2, 1/2)

$CaCu_5$ structure is obtained by stacking layers along [0001] axes in sequence ABABAB.... Layer A consists of one Ca (or Sm) atom and two Cu (or Co) atoms. Layer B consists of three Cu (or Co) atoms.

The rhombohedral Sm_2Co_{17} compound has Th_2Zn_{17} type structure and belongs to space group R3m. Its crystal structure is shown in figure 2.2. One unit cell consists of 57 atoms (three formula units of Th_2Zn_{17}). There are four crystallographically distinct Zn (or Co) sites and one Th (or Sm)site. There are six Th (or Sm) atoms in (c) site and 51 Zn (or Co) atoms in (d), (f), (h), and (c) sites. The locations of the atoms are listed in Table 2.2.

From figure 2.2 it can be seen that each unit cell consists of a six layer repeat structure perpendicular to the c axis. The locations of the layers are z=0, 1/6, 1/3, 1/2, 2/3, 5/6. The projection of the layers on the basal plane along <0001> is shown in figure 2.3. In figure 2.3 parallelogram $B_1A_3B_4C_3$ is the projection of an unit cell of Th_2Zn_{17} and parallelogram $B_1B_2C_3C_2$ corresponds to that of $CaCu_5$ unit cell. The big circles represent the Th (or Sm) atoms in layers of z=0, 1/3, 2/3 and the small circles represent the Zn (or Co) atoms in these layers. These three layers correspond to the A layer in $CaCu_5$ structure. Black points represent the Zn (or Co) atoms in the layers at z=1/6, 1/2, 5/6 which correspond to the B layers of CaCu5 structure. The B1 site (and its equivalent sites A_3, B_4, C_3) in the basal plane is occupied by a Ca (or Sm) atom in CaCu5 structure, but is replace by a pair of Zn (or Co atoms) (dumb-bell) in Th_2Zn_{17} structure. The dumbbell pairs orient perpendicular to the basal plane and the dumbbell atoms are positioned away from basal plane by ±0.097c. Same substitution happens for layers at z=1/2 and 2/3. The dumbbells are located at site B2 in layer z=1/2 and at B3 in layer z=2/3.

Thus the Sm_2Co_{17} structure is derived from $SmCo_5$ structure by the ordered substitution of each third Sm atom in the basal plane with a dumbbell pair of Co atoms[22]. When these substituted layers are stacked in the sequence abcabc, the Th_2Zn_{17} type rhombohedral structure results. If the stacking sequence is ababab, then Th_2Zn_{17} type hexagonal structure is formed. If, instead, the stacking sequence is random, for homogeneous phases in the composition range between 1-5 and 2-17, the disordered $TbCu_7$ structure results[23].

From the above discussion it follows that the R_2Co_{17} intermetallic compounds have one of the following structures:

(a) $TbCu_7$ type (disordered);

(b) Th_2Ni_{17} type (ordered);

(c) Th_2Zn_{17} type (ordered);

depending upon participating R element. Th_2Ni_{17} and Th_2Zn_{17} type structures are superstructures of the $TbCu_7$ type structure. The relations between their a and c parameters are:

$c(Th_2Zn_{17}\ type) = 3/2c(Th_2Ni_{17}\ type) = 3c(TbCu_7\ type)$

$a(Th_2Zn_{17}\ type) = a(Th_2Ni_{17}\ type) = \sqrt{3}a(TbCu_7\ type)$.

The Th_2Ni_{17} type Sm_2Co_{17} phase was found only in splat-cooled samples indicating either that it is a high temperature phase or metastable over the entire temperature range.

2.3. Magnetism in RE-TM Alloys

The RE is characterized by its 4f electron shell which is only partially full. The 4f electrons in the RE atoms are shielded by the electrons in the 5s and 5p shells. The magnetic moment of RE atoms is a composite of both orbital and spin contributions of 4f electrons. The total angular momentum is represented by J, where J=L-S for light rare-earth (total number of f electrons less than 7), and J=L+S for heavy rare-earth (total number of f electrons more than 7). Because of the localized 4f configuration, the magnetic moment of the 4f shell in a solid is similar to that of free ion. The exchange interaction between RE atoms is indirect (RKKY interaction). The coupling of the f electrons is through polarization of the conduction electrons.

Magnetic moments of ferromagnetic 3d transition elements are unlike those of the 4f series in that the magnetic electrons are nonlocalized. In Co, the orbital angular momentum is mostly quenched and the contribution to the total magnetic moment is essentially from the electron spin of the unpaired 3d electrons.

In RE-TM compounds, the principal exchange interaction is that between transition metal atoms. It is due to direct overlap of the 3d shells on neighboring sites. This direct interaction is usually ferromagnetic, but depends sensitively on the interatomic spacing. In $RECo_5$ and RE_2Co_{17} compounds, the Co interatomic distances are comparable to those in pure Co metal, resulting in strong 3d correlations. The ferromagnetic interaction is strongest for cobalt, and significantly weaker for iron or nickel.

The interaction between transition metal atom and rare-earth atom is indirect[24][25]. As a result of this interaction, the rare-earth 4f and transition metal 3d spin moments are

always aligned antiparallel in the RE-TM compounds[26][27]. This antiparallel coupling can be explained by invoking the RKKY interaction in which the 3d-4f coupling occurs indirectly via polarization of the s conduction electrons[24][28]. The interaction Hamiltonian is[28]

$$H_{RE\text{-}TM} \propto J_{sf} J_{sd} \sum_{i,j} F(2k_F R_{i,j}) S_i^{RE} S_j^{TM}$$

where J_{sf} and J_{sd} are effective 4f-s and 3d-s exchange integral, S_i^{RE} and S_j^{TM} are the spin operators for local RE and TM 3d spins at lattice sites i and j separated by R_{ij}, k_F is the Fermi wave vector, and $F(x)=(x\cos x-\sin x)/x^4$ is the RKKY oscillatory type function. According to this scheme, 3d electrons negatively polarize the conduction electrons in the alloy. Then a positive interaction between the conduction electrons and RE 4f electrons causes the spin of the 4f electrons to be antiparallel to that of the Co atoms.

A more realistic description of 3d-4f coupling was proposed by Campbell[25][29]. The interaction between 3d(TM) and 4f(RE) electrons proceed through 5d electrons of RE. The intratomic 4f-5d interaction is ferromagnetic arising from an ordinary 4f-5d exchange. The interatomic 5d-3d interaction is antiferromagnetic when the 5d band is less than half full and the 3d band is more than half full which is the case for RE-TM compounds. Therefor, the RE and TM spins are coupled antiferromagneticly.

Because the direct overlap between the 4f shells of adjacent RE atoms is quite negligible, the exchange coupling between RE atoms is indirect, proceeding via spin polarization of the conduction electrons (RKKY type). R-R interaction in the RE-TM intermetallic compounds of concern here are generally quite small by comparison with R-T and T-T interactions, and are neglected accordingly.

Because the RE and TM spins are antiparallel, the magnetizations of RE and TM sublattices couple parallel for light rare-earths (J=L-S) and antiparallel for Gd and heavy rare earths (J=L+S)[27]. Thus the alloys of Fe or Co and the light rare earths (LRE) have a ferromagnetic structure and the alloys of Fe or Co and heavy rare earths (HRE) are ferrimagnetic with a reduced total magnetization. At room temperature, a large portion of the moment observed in the LRE-Co compounds is contributed by the cobalt atoms. Because of this, the Co enriched LRE-Co compounds show higher saturation.

2.4. Magnetocrystalline Anisotropy in RE-TM Compounds

In $RECo_5$ compounds, Co sublattice makes a large contribution to the uniaxial anisotropy, as indicated by the large uniaxial anisotropy measured on $RECo_5$ compounds involving nonmagnetic RE such as YCo_5, $LaCo_5$, and $CeCo_5$ at room temperature[30]. In the other $RECo_5$ compounds, the total anisotropy includes the contribution of the RE's as well. The cobalt sublattice favors large, positive values of K1 and hence an easy axis, and the rare earth sublatttice favors an easy plane for Pr, Nd, Tb and Ho, but easy axis for Sm. Because the RE sublattice moment decreases rapidly with the increase of temperature, the contribution of the Co sublattice dominates at high temperature. As a result, at high temperature, easy axis anisotropy is seen for all of the $RECo_5$ compounds. For YCo_5 and $CeCo_5$, uniaxial anisotropy is maintained for the entire temperature range. For most of the $RECo_5$ compounds with magnetic rare earth element, except for $SmCo_5$, the easy axis anisotropy changes to easy cone or easy basal plane anisotropy at some low temperature.

In RE_2Co_{17} compounds, the higher Co content leads to increase in $4\pi M_S$ and decrease in H_A because the dumbbell cobalts contribute additional moment and an easy plane anisotropy. Except for Sm, Er, and Tm, all other RE_2Co_{17} compounds are characterized by easy plane anisotropy in room temperature. The cobalt sublattice in RE_2Co_{17} compound contributes negative K1 hence favoring easy plane.

Both $SmCo_5$ and Sm_2Co_{17} show uniaxial anisotropy because of the strong contribution of the Sm sublattice to the uniaxial anisotropy[31]. The anisotropy field of $SmCo_5$ at room temperature is 400 kOe compared to that of 250kOe for $GdCo_5$ and around 170kOe for other $LRECo_5$. For Sm_2Co_{17}, anisotropy field is reported around 100 kOe.

Even though the magnetocrystalline anisotropy of the $RECo_5$ and RE_2Co_{17} compounds is determined by contributions from both cobalt sublattice and RE sublattice, a single-ion model performed with respect to the RE ion successfully described the observed anisotropy(31). The success of this model in describing the anisotropy relies on the fact that (1)the moments of the RE ions can be treated as localized because of the shielding of the 4f electrons by the 5s and 5p electrons, and (2)the strong 4f spin-orbit coupling in RE leads to a well defined total angular momentum J and associated magnetic moment -gJ in the ground state. The model treats the crystal-field splitting of the RE ion together with a mean field description of the RE-Co exchange. The contribution of RE ion is described by a Hamiltonian that includes the crystal-field and exchange interactions as following

$$H_R = H_{CF} + g\mu_B \mathbf{J}\,\mathbf{H}_{ex}$$

The second term represents the exchange interaction of the RE ion with the exchange field H_{ex}. The first term is the crystal-field Hamiltonian and has the general form

$$H_{CF} = \sum_{n=0}^{6} \sum_{m=0}^{n} B_n^m O_n^m$$

where O_n^m are the Stevens angular momentum operator equivalents and coefficients B_n^m are given by

$$B_n^m = \theta_J^n \langle r^n \rangle (1-\sigma_n) K_n^m A_n^m$$

where θ_J^n are the Stevens factors (σ_J, β_J for n=2,4, respectively), $\langle r^n \rangle$ is the r^n radial matrix element for the 4f shell, σ_n are shielding factor and K_n^m are numerical constants.

Coefficients A_n^m describe the crystal field produced by environment. In the point charge model, A_n^m are given by

$$A_n^m = (4\pi e/(2n+1))\Sigma q_i Y_n^m(\theta_i,\varphi_i)/R_i^{n+1}$$

where q_i are charges associated with atomic sites (θ_i,φ_i,R_i).

The number of terms in the expansion is limited by the point symmetry of the rare earth site. Considering the point symmetry of the rare earth site in $RECo_5$ and RE_2Co_{17}(D_{6h} and C_{3v} respectively), number of terms in H_{CF} can be reduced to 4 and 6 terms respectively. As a first order attempt, only the dominant term, $B_2^0\ O_2^0$, is important in the crystal field potential. Then the Hamiltonian has the form

$$H_R = B_2^0\ O_2^0 + g\mu_B\ \mathbf{J}\ \mathbf{H}_{ex}$$

The magnitude and sign of B_2^0 are determined by the environment at the RE site and ground state configuration of the RE ion. Only the RE near neighbors are considered in the calculation and the electric charge on the Co atom is considered to be near zero.

Eigenvalues are then calculated for the Hamiltonian for cases where the exchange field is parallel and normal to the c-axis. Values of exchange field can be estimated from experiment. The sign of the term B_2^0, which is the sign of product of σ_J and A_2^0, determines whether the rare earth has easy axis or easy plane anisotropy. The sign of A_2^0 is decided by the crystal structure, but that of σ_J depends on the shape of the 4f charge distribution. The sign of σ_J for Sm is positive which is opposite to that for Pr, Nd, or Tb. For a crystal structure with negative A_2^0, which is the case for $CaCu_5$ and Th_2Zn_{17}

structure, easy axis anisotropy exhibits when RE=Sm, but easy plane anisotropy when RE=Pr, Nd, or Tb.

Extended from this model, the magnetic anisotropy associated with the samarium sublattice has been evaluated for $SmCo_5$ over the temperature range 4-970K[32]. It correctly predicts the easy direction of magnetization and the free-energy values calculated from 4 to 970K are in fair agreement with experiment.

2.5. Pair Model of Magnetic Anisotropy and Dipolar and Pseudodipolar Interactions

According to the pair model, the total energy of the system is the sum of a series of terms each related to a pair of nearest-neighbor atoms[33]. The interaction energy between two atoms depends generally on the relative orientations of the bond and the spins of the two atoms. In order to explain magnetic anisotropy we may assume that the pair energy is dependent on the direction of magnetic moment, ø, as measured from bond direction. The pair energy is then expanded in form of Legendre polynomials of even order:

$$E(\cos\text{ø}) = g + l(\cos^2\text{ø} - 1/3) + q(\cos^4\text{ø} - 6/7\cos^2\text{ø} + 3/35) + \ldots \quad \text{-----(2.1)}$$

The first term, g, which is independent of ø, includes the chemical binding energy between the two atoms, which can be as large as 10^{-11}erg(several eV) and is a constant for a given length of bond[34]. The g term also includes the exchange energy, which is dependent only on the angle between neighboring atomic moments, independently of their orientation relative to their bond direction.

The second and third term are the dipolar and quadrupolar terms respectively. One of the sources for the dipolar term is magnetic dipolar interaction. The dipolar interaction energy of two magnetic dipoles m_i and m_j separated by r_{ij} is given by

$$U_{ij} = f(r_{ij})[m_i.m_j - 3(m_i.r_{ij})(m_j.r_{ij})/r_{ij}^2] \quad \text{----(2.2)}$$

where $f(r) = 1/r^3$. In most cases, the magnetic dipolar interactions are too weak to cause the observed anisotropies.

The main source of the dipolar terms is the combined effect of the exchange interaction, the spin-orbit interaction, and the coulomb interaction between atoms, provided there is a small amount of orbital magnetic moment remaining unquenched by the crystalline field(33). A part of the orbit of each atoms will follow the orientation of the magnetic spin due to the spin-orbit coupling. This alters their overlapping status and leads to a change in the Coulomb interaction energy. For this reason, the dipolar term is called pseudodipolar interaction. It still has the form of eq. 2.2, but here f(r) are expected to be shorter ranged than for true dipolar interaction and to differ in strength and perhaps in sign for different types of pairs.

CHAPTER 3 EXPERIMENT

3.1. Synthesis of Films

The films reported in this thesis were synthesized by RF glow discharge sputter deposition. RF sputter deposition is a common method for preparing thin films for research, development, and production purposes and is well documented in the literature[35][36]. It has the advantage that the deposition processes can be very well controlled by many parameters.

The vacuum system used for synthesizing the films consists of a stainless steel chamber and a cryopump aided by an ion pump. The base pressure could be brought to the 10^{-8}torr range and normally operated in the low 10^{-7} torrs. The chamber was normally baked for at least 24 hours before starting sputter deposition.

Two type of targets were used for film deposition. The first was "bar type" which was commercially available TDK 2-17 type bar magnet. The composition of the original bar magnet target was:

ELEMENT	ATOMIC %
Sm	14.2
Co	55.5
Fe	20.1
Cu	7.8
Zr	2.4

To modify the composition of films, a sandwich of Fe stripes and TDK bar magnets was used as target. Another type was the "button target" made from arc melting in a vacuum chamber in an inert atmosphere from pure elements(at least 99.9% pure). The benefit of the button targets is that we could change the composition of films by changing the composition of target instead of changing the sputtering parameters. Although composition of the films deposited from the same set of targets can be varied through controlling the sputtering parameters, sometimes comparison between the films with different composition but deposited at same conditions were needed.

The films were deposited on polycrystalline Al_2O_3 corundum substrates. Substrates were heated by a quartz lamp. The preheating temperature of the substrate prior to the sputter deposition depended on the power supplied to the lamp and ranged from room temperature to 900k. The actual surface temperature of the substrates during sputter deposition were 50 to 80 degree higher than the preheating temperature due to plasma heating. The same quartz lamp was also used for post deposition heating or annealing. To control the heating rate, a custom made temperature controller system was used on some occasions. It used INTEL's 8052AH microcontroller to control the Kepco power supply which powered the quartz lamp. Aided with MCS BASIC-52, the controller was programmed to increase or decrease the power supplied to the lamp in desired rate.

An in-plane magnetic field was applied using various permanent bar magnets in a yoke arrangement. The applied field ranged from 12 Oe to 5.0 kOe and was highly parallel to the substrate plane.

The sputtering gases used were Ar, Xe, or their mixtures. Because the magnetic properties of Sm-Co type film are extremely sensitive to the presence of Oxygen in the sputter deposition environment, the sputtering gas was cycled through the vacuum chamber for the duration of deposition in order to maintain the system purity. The flow and the pressure of the gas was controlled by an MKS mass flow controller and an exhaust valve respectively. Normal flow rate was around 1.0 sccm. The sputter gas pressure ranged from 20 mTorr to 150 mTorr.

The sputtering rate was controlled by input RF power and gas pressure providing that the substrate target geometry arrangement was fixed. One of the advantages of the sputtering technique is that the rate of deposition remains constant with time if the RF power and gas pressure do not vary. These conditions were attained in our system by using an automatic pressure controller and regulated power supply. The deposition rate in our system ranged from 0.1 μm per minute to 2.0 μm per minute. The thickness of the films ranged from 500 Å to 5 μm.

The special magnetic properties of the film magnets were achieved through process control, which includes substrate temperature during sputtering, sputter gas pressure, and type of sputter gas. There are two methods of sputter deposition differing in the way of crystallizing the film magnets. First method is subsequent crystallization: the film magnets are first sputter deposited in amorphous form and subsequently crystallized through heat treatment. The second method is direct crystallization: the film magnets are directly crystallized by sputter deposition onto substrates maintained at proper high temperature.

3.2. Characterization of Films

The magnetic measurements were made using a Vibrating Sample Magnetometer. Magnetic fields up to 18kOe were provided by an iron core magnet and up to 90kOe by a superconducting magnet. Most of the measurements were done at room temperature. Low temperature measurements were also performed for some samples (down to 5 K). Hysteresis loop measurements were controlled by a personal computer and all the scanning and data acquisition procedures were automated. The size of the sample for measurement was around 0.090 cm^2 and gave magnetic moments in the order of 10^{-2} to 10^{-3}emu. The substrate had a diamagnetic contribution in the order of 10^{-6}emu/gm and was corrected for. The typical signal to noise ratio was less than 3%.

Composition of the film was measured through a scanning electron microscope coupled with an Energy Dispersive X-ray spectrometer. Details of the technique are well documented in the literature(37). The analyzer included a liquid Nitrogen cooled Si(Li) detector, a multi-channel analyzer, and a dedicated computer for data acquisition and analysis. For our samples, elements Sm, Co, Fe, Cu, and Zr were involved. The electron excited x-ray K_α lines of Co and Fe and the $L\alpha$ line of the Sm were used to determine the composition.

The crystal structure, lattice parameters a and c and film X-ray density were determined using an X-ray diffractometer coupled with a Si(Li) detector. An MCA and a computer were coupled with the system for data acquisition and angle scanning control. Cu $K\alpha_1$ radiation were used for diffraction analysis. Precise lattice parameters were determined by using a fitting procedure designed in this lab(1).

The thickness of the films was usually determined by the film's mass, area, and density. The major contribution to error came from the density measurement. For accurate determination of the film thickness, scanning electron microscope was used to measure actual thickness from the film edge. The density was then calculated through the mass and volume of the film and was compared with the X-ray density.

The scanning electron microscopy was also used to study the film morphology. The resolution was 50 Å which was normally enough to observe the grains in our films.

CHAPTER 4 SYNTHESIS OF Sm-Co BASED 2-17 TYPE FILMS

4.1 Introduction

A sputter deposition method was developed previously which allowed the synthesis of Sm-Co type film magnets with $TbCu_7$ type structure [6][5]. The crystallites of these films had their easy magnetic axes aligned in the film plane. The films were synthesized in one step through the deposition of the Sm-Co materials onto heated substrates without any post deposition thermal treatment. The alignment was achieved only through thermallized sputtering and proper substrate heating temperature[7]. The deposition temperature had to be low enough to prevent the c-axes of crystallites from growing skewed out of the film plane.

A similar method was successfully used here to synthesize Sm-Co based films with rhombohedral 2-17 Th_2Zn_{17} type structure[10]. The Th_2Zn_{17} structure is a superstructure of $CaCu_5$ type structure resulting from ordered substitution of one RE atom with a pair of TM atoms for every three unit cells of the $CaCu_5$ structure. However,

when this substitution is not ordered, the disordered $TbCu_7$ structure results. Detailed description of crystal structures are already given in chapter 2 of this thesis.

The 2-17 type films were synthesized from Fe enriched TDK targets through thermallized sputtering onto substrates heated to 400-500 °C. Fe concentrations of the films were up to 30 at.%. The crystal structure of these Fe enriched films was found to be rhombohedral 2-17 Th_2Zn_{17} type. For Fe concentration of around 20 at.%, the films could not be formed in the ordered 2-17 phase. Instead, these lower Fe concentration films formed in the disordered $TbCu_7$ type structure. The Fe enriched rhombohedral 2-17 type films exhibited unusually strong (220) texturing with $I(113)/I(220) < 1/40$, for out of plane c axes to in plane texture, and $I(300)/I(220) < 1/50$, for relative c axes in plane textures.

4.2. Experiment Details

In order to obtain higher Fe concentration in the films, various portions of the TDK target of composition $Sm(Co_{0.65}Fe_{0.24}Cu_{0.24}Zr_{0.02})_{6.10}$ were replaced by 99.99% pure Fe. The rectangular TDK pieces were sandwiched together with Fe sheets as shown in figure 4.1. The Fe concentration of the films was adjusted by changing the thickness of the Fe sheets in the targets. Direct crystallization of the film magnets was carried out through thermallized sputter deposition onto substrates heated to 400-500 °C. The various films synthesized were in the 4 μm thickness range. A sputtering gas of Ar50%Xe mixture and pressure of 60 mTorr were used for sputter deposition. This condition assured that the sputtered atoms arriving at the substrate had lost most of their initial kinetic energy through collisions with the gas phase and was necessary to obtain highly textured Sm-Co 2-17 type films (7).

4.3. Results and Discussion

Figures 4.2 show x-ray diffraction trace of an Fe enriched film (sample A) with an Fe concentration of 30 at.% with composition $Sm(Co_{0.55}Fe_{0.35}Cu_{0.08}Zr_{0.02})_{6.50}$. As a result of unusually strong reflection at 43.00°, the Y axis is log scale to accentuate the smaller peaks. The lines are indexed according to the hexagonal transformation of rhombohedral Th_2Zn_{17} structure and is explained as following.

As stated in chapter 2, in the interested range of Sm concentration, possible crystal structure of Sm-Co based compounds are Th_2Ni_{17}, Th_2Zn_{17}, and disordered $TbCu_7$ type. They are all $CaCu_5$ derived structures. Especially, Th_2Ni_{17} and Th_2Zn_{17} type structures are superstructures of the $TbCu_7$ type structure. As a result, the close resemblances of their X-ray diffraction patterns are expected. Tables 4.1-4.3 list the diffraction lines of each structure with their spacing d, relative intensity and the (hkl) indexing of the reflecting planes. The index for rhombohedral 2-17 structure is of its hexagonal transformation and will be used in that for the rest of this thesis. As shown in table 4.4, for every diffraction line of $TbCu_7$ structure, a corresponding fundamental diffraction line of the hexagonal and rhombohedral 2-17 structures can be found. From the formula for d spacing and the relations between a and c axes, one can easily obtain the transformation formula of index (hkl) as following:

$l(Th_2Zn_{17}\ \text{type}) = 3\ l\ (TbCu_7\ \text{type})$

$(h^2+hk+k^2)\ (Th_2Zn_{17}\ \text{type}) = 3(h^2+hk+k^2)\ (TbCu_7\ \text{type})$

and

$l(Th_2Ni_{17}\ type) = 2\ l\ (TbCu_7\ type)$

$(h^2+hk+k^2)\ (Th_2Ni_{17}\ type) = 3(h^2+hk+k^2)\ (TbCu_7\ type)$

The corresponding transformation matrices are given as following:

$$\begin{bmatrix} h \\ k \\ l \end{bmatrix}_{2\text{-}17(Rhom.)} = \begin{bmatrix} 1 & -1 & 0 \\ 1 & 2 & 0 \\ 0 & 0 & 3 \end{bmatrix} \begin{bmatrix} h \\ k \\ l \end{bmatrix}_{1\text{-}5(TbCu_7)}$$

and

$$\begin{bmatrix} h \\ k \\ l \end{bmatrix}_{2\text{-}17(Hex.)} = \begin{bmatrix} 1 & -1 & 0 \\ 1 & 2 & 0 \\ 0 & 0 & 2 \end{bmatrix} \begin{bmatrix} h \\ k \\ l \end{bmatrix}_{1\text{-}5(TbCu_7)}$$

In addition to these transformation related lines, the ordered phase exhibits a higher density of lines (see table 4.4). These additional superstructure lines can be used to identify the different structures.

Due to texturing, not all the diffraction lines were present in our film sample. In table 4.5, a listing of the 2Ø values of diffraction lines obtained from sample A is given. Also given are indices for each line that is possible to be indexed based on Th_2Ni_{17}, Th_2Zn_{17}, and disordered $TbCu_7$ type structures. The indexing is obtained through a fitting procedure developed in this lab[1]. As expected, most of the lines can be indexed for all three structures following the transformation formula mentioned above. The Th_2Ni_{17} structure

is the only one that accounts for all the observed lines including the 28.45° reflection and is identified as the crystal structure of our films.

The weak broad shoulder at around 41.5° to the left of the strongest reflection line and the line at 45.0° belong to 1-5 phase, namely (200), (111), and (002). The (200) and (111) lines are the two strongest reflections of 1-5 phase. These reflections indicate that small amounts of 1-5 phase exist in the film.

The diffraction trace shows that the film is strongly textured, with the c axes of the crystallites aligned onto the film plane, as indicated by the very large intensity of the (220) reflection compared with that of other reflections. The ratio of out of plane reflection (113) to the inplane (200) is less than 2.5%. However, the lines belonging to the minor 1-5 phase do not show such texturing as evidenced by the presence of the (200), (111), and (002) reflections. This can be interpreted as due to the presence of 1-5 phase primarily in the grain boundary regions.

The x-ray diffraction trace of a film (sample B) with a lower Fe concentration of 20.1 at.% with composition $Sm(Co_{0.65}Fe_{0.24}Cu_{0.09}Zr_{0.02})_{6.50}$ is shown in figure 4.3. All the lines observed could be fitted to the $TbCu_7$ type disordered 2-17 phase with lattice parameters a=4.847 Å and c=4.135 Å. No lines corresponding to a second phase could be detected.

Both sample A and sample B were deposited on substrates preheated at 400 °C. They have similar Sm concentration at 13.3 at.%. However, sample A was synthesized using Ar50%Xe gas at pressure of 60 mTorr from Fe stripe modified targets and sample B was synthesized at 30 mTorr pressure of the same gas mixture from unmodified TDK target. The low sputtering gas pressure for the latter was necessary to obtain lower Sm

concentration than that of target. The Sm concentration of the target is 14.2 at.%. Previously it was shown that the Sm concentration of the films increases when the pressure increase[38].

It is rather surprising that the increase in the film Fe concentration alone has allowed the nucleation and growth of ordered 2-17 and 1-5 phases in the films. For Fe enriched films, at a total Sm concentration of approximately 12 at.%, only the ordered 2-17 phase could be detected. In contrast, for films with lower Fe concentration, for Sm concentration in the 12-15 at.% range, the Th_2Ni_{17} or Th_2Zn_{17} type ordered 2-17 phases failed to form. Instead, the crystal structure observed was $TbCu_7$ type disordered 2-17 in these nonenriched films. The two phase form had been observed for lower Fe concentration films only at Sm concentrations of around 15.5 at.%. But the phases were $TbCu_7$ type disordered 2-17 and $CaCu_5$ type 1-5.

It should be noted that the films with lower Fe concentration of about 20 at.% and higher Sm concentration of around 15 at.% were synthesized such that all the crystallites had their c axes aligned onto the film plane. This was indicated by the absence of reflections from planes having nonzero l indices. However the unusually strong (220) texturing observed for Fe enriched films, was not observed for the $TbCu_7$ type films even in the case where there was total alignment of the crystallographic c axes in the film plane.

In the Sm-Fe phase diagram, the 1-5 phase is absent. This indicates that Fe has very limited solubility in $CaCu_5$ structure. Neutron diffraction studies have shown that Fe preferentially occupies the dumbbell sites when added to the Th_2Ni_{17} type Sm_2Co_{17} compounds [39]. Thus it is easy to understand why the increase in the film Fe concentration has allowed the ordered 2-17 phase formed in the films.

The as sputtered demagnetization behavior of the Fe enriched films was quite poor with significant drop in the $4\pi M$ values being seen on entering the second quadrant. Such films showed intrinsic coercivities less than 3.0 kOe and maximum energy products observed did not exceed 12 MGOe. However, after post deposition heat treatments at temperatures in the 400-500 °C range for 1-2 h, it was found that the second quadrant drop could be mostly eliminated, and coercivities raised to above 5 kOe. In figure 4.4, the hysteresis loops of film before and after the post deposition heat treatment for 2 hours at 450 °C are shown. This film was first crystallized through sputter deposition onto substrates preheated to 400°C. After post deposition heat treatment, the films showed high energy products in 19-20 MGOe range and saturation magnetization of 11.5-12.0 kG range. Similar values of energy products have been obtained in films with lower Fe concentration of around 20 at.% and higher Sm concentration of 14-15 at.%. However, the saturation magnetization of Fe enriched films were substantially higher than the 9-10 kOe of the nonenriched films of 9-10 kG. The increase of saturation magnetization is due to the higher TM content and higher percentage of Fe in TM content[40].

In conclusion, the Fe enrichment of the films has made it possible to synthesize films with the Th_2Zn_{17} type majority phase and a minor $CaCu_5$ type 1-5 phase. At similar crystallization temperatures and Sm concentrations, films with lower Fe concentration formed in $TbCu_7$ type disordered structure. The saturation magnetization of Fe enriched films is substantially higher than that of nonenriched films. The energy products of the Fe enriched films are in the 19-20 MGOe range after post deposition heat treatment. Unusually strong (220) texturing were present in the Fe enriched 2-17 films, even in the absence of total alignment of c axes in the film plane.

CHAPTER 5 MAGNETIC ANISOTROPY IN Sm-Co BASED FILMS

5.1. Introduction

Induced anisotropy in magnetic thin films has been the subject of many investigations for a long time. Especially, the magnetic anisotropy in rare-earth-transition-metal amorphous alloys has potential application in storage technology. Anisotropy in these materials is closely related to their preparation conditions and must be due to some deviation from isotropy in arrangements of atoms in the amorphous films. Yet the structural anisotropy built in by the growth process is far from well understood. Understanding of the formation of this anisotropy also helps us to understand the fundamental growth process during the film deposition. Thus the subject is of both technological and scientifical interest.

Magnetic anisotropy is observed in amorphous rare-earth-transition-metal (a-RE-TM) films produced by sputtering and vapor deposition. Uniaxial anisotropy with the easy magnetization direction perpendicular to the film plane has been found to be a common characteristic for most a-RE-TM films[41]. However, with the presence of in-plane magnetic field during deposition process, an in-the-film-plane uniaxial anisotropy is formed with easy magnetization direction parallel to the direction of field applied during deposition [11] [12][13]. Various mechanisms have been proposed to explain the perpendicular anisotropy in a-RE-TM films. Among them are the pair ordering model[42][43][44], the single-ion model[45], the bond orientational anisotropy[46][47], and growth-induced anisotropy[48]. The origin of in-the-film-plane anisotropy has also been explained by pair ordering model[49], local structural model or a combination of both [14][15]. In the latter case, the formation of the pair ordering has been related to the field annealing of ferromagnetic alloys. But in fact, the mechanism that causes the

directional structure in field annealed alloys is different from that of films deposited in a magnetic field. The reason is that the structure in films is formed during the film growth process, which only involves the surface layer, but in field annealed alloys, it is basically a bulk process(50). The mechanism of in-the-film-plane anisotropy is more closely related to that of perpendicular anisotropy. Both anisotropies are formed during the growth process and their mechanisms must coexist even if they are different.

In this work, in an attempt to better understand the formation and the physical origin of the anisotropy in a-RE-TM films, a study was performed on Sm-Co amorphous films. The magnetic properties were studied systematically as a function of concentration and deposition parameters. Especially, the dependence of in-the-film-plane anisotropy on in-plane field applied during deposition was studied. Post deposition annealing was performed in an attempt to reveal the physical origin of the anisotropy. With a large in-plane applied field H_S present, a well defined and large in-the-film-plane magnetic anisotropy was obtained in amorphous SmCo films. The in-plane anisotropy depended essentially on the applied field H_S and Sm concentration. Both in-the-film-plane, and perpendicular anisotropy were present in the sputter synthesized SmCo films depending on the film preparation conditions. Different sources of anisotropy were distinguished in these films. The physical origin of in-the-film-plane anisotropy was explained as directional pair ordering. This work shows that the perpendicular anisotropy can not be explained by directional pair ordering, instead, it was only formed in films synthesized through thermallized sputtering and was caused by growth induced structure. A much stronger third type of anisotropy was present in films deposited at a temperature higher than the ambient, but below the crystallization temperature. The easy direction for this anisotropy was in the film plane with no preferred direction within the film plane. It is concluded that surface induced short range ordering was the origin of in-the-film-plane

anisotropy observed in amorphous films deposited in a magnetic field. The formation mechanism is different from that of the short range ordering induced by field annealing.

5.2. Experimental Details

The in-plane magnetic field, H_S, was applied by using various permanent magnets in a yoke type arrangement. The magnitude of applied field ranged from 12 Oe to 5.0 kOe and its direction was highly parallel to the substrate plane along the width. The yoke arrangement and large substrate to target distance assured minimum disturbance of the plasma by the applied field H_S during sputtering.

Button targets made through arc melting in an inert atmosphere from pure elements of Sm and Co (at least 99.9% pure) were used. The benefit of using button targets is that we can obtain films with various Sm concentration but deposited at the same sputtering conditions. Three button targets were arranged in a line parallel to the substrate. Each button target had different Sm content and was arranged in order. This arrangement resulted in a composition gradient across the length of the film. The 5 cm long film was then cut into small pieces of about 3 mm X 3 mm. Three to four pieces were used as samples for further study. The composition variation in the sample piece did not exceed 1%.

The substrate temperature T_{sub} during the deposition was controlled by a heater lamp and water cooling tube. It ranged from 50 °C to 600 °C. To obtain a T_{sub} below the room temperature, liquid Nitrogen was passed through the water cooling line instead of water. A T_{sub} of -50 °C was obtained by this method.

Hysteresis loops were measured with the direction of applied field in-plane parallel to H_S, in-plane perpendicular to H_S, and perpendicular to the film plane.

5.3. Experimental Results and Discussion

5.3.a. Film Morphology and Structure

The synthesized Sm-Co films were visually shiny. Films examined by SEM proved to be dense and featureless at all compositions from 10 to 37 at.% Sm.

X-ray diffraction measurements showed no sign of crystallinity for films deposited at room temperature for Sm concentration range from 9.0 to 37 at.%. The X-ray diffraction scan for a film containing 19 at.% Sm is shown in figure 5.1 . An average radial spacing d of 2.27 Å is obtained by measuring the location of the 2Ø peak maximum.

5.3.b. Characteristics of the Hysteresis Loop

A systematic study of the in-plane M-H loops revealed the following general characters. For $H_S > 500$ G, films were found to exhibit rectangular hysteresis loops measured along the in-plane parallel to H_S direction, and inclined hysteresis loops along the in-plane perpendicular to H_S direction. Thus the direction H_S applied became the direction of the easy axis.

With a large H_S of 5.0 kOe, films with very well defined and large in-plane anisotropy have been synthesized. The typical M-H loops for H_S=5.0 kOe are shown in fig. 5.2. The film was synthesized at pressure of 70 mTorr and rate of 2Å/sec. For the loop measured

along the hard direction, opening of the loop is undetectable, and the loop along easy axis is a perfect rectangular, which indicates that the easy axis is very well defined and no dispersion of the easy axes is present. The M-H loop of these films obtained along the normal to film plane direction also shows no hysteresis.

Works done elsewhere have shown that among various a-TM-RE thin films, SmCo, SmTiFe and TbFeCo thin films exhibit large in-the-film-plane anisotropy constants K_u = 10^5-10^6 erg/cm^3, but with a large opening of the M-H loop along the in-plane hard axis (11)(12)(13), indicating a dispersion of the easy axes. A well defined in-plane uniaxial anisotropy was reported for a-CoDyZr and a-CoTi thin films but with much smaller in-plane anisotropies, 10^3 erg/cm^3 (51). In our work, a well defined in-the-film-plane anisotropy of exceptionally high value of $K_u = 3.3 \cdot 10^6$ erg/cm^3 has been obtained with H_S=5.0 kOe. This is the largest value ever reported for in-the-film-plane anisotropy induced during the deposition process.

The general cases are shown in Fig. 5.3, in which the ratio of remanence B_r over $4\pi M_S$ is plotted against the Sm concentration for various H_S. The opening of the M-H loop (which is indicated by the ratio of the remanence B_r over $4\pi M_S$) along hard axis is relatively large when the films were synthesized with H_S of 1.8 kOe or less especially with high Sm concentration and it closes up for films synthesized with H_S=3.0 KOe. For the films synthesized with H_S less than 600 Oe, the M-H loops along easy axis become S-shaped and the loops along easy and hard axes were coincident so that there was almost no in-plane anisotropy present.

5.3.c. Magnetization

The variations of $4\pi M_S$, H_k, and K_u were studied as a function of the Sm concentration and the H_S value for a series of amorphous Sm_xCo_{1-x} films sputtered under similar conditions at a fixed sputter gas pressure of 100 mTorr Ar.

The values of $4\pi M_S$ obtained were independent of the deposition parameters over the composition range from x=0.10 to 0.37. Figure 5.4 shows the variation of $4\pi M_S$ with the Sm concentration x at room temperature. In the range $0.08 < x < 0.35$, the $4\pi M_S$ varies with x as follows:

$$4\pi M_S = 17.1 - 37.3x \text{ (kG)}$$

The films were found to be paramagnetic at room temperature for $x > 0.41$. This is consistent with the fact that the Curie temperature for amorphous SmCo films of $x > 0.4$ is below the room temperature[52].

5.3.d. Induced Anisotropy

Figure 5.5 shows the variation of K_u with atomic percentage of Sm for films synthesized with different values of H_S. The K_u here was calculated from the area enclosed by the initial M-H curves measured in-plane parallel and perpendicular to the easy axis. The K_u represents the energy required to rotate the magnetization from in-plane easy direction to hard direction. As shown in figure 5.5, for H_S below 5.0 kOe, the K_u exhibits a broad maximum around x=0.25 and rapidly decreases for both higher and lower Sm concentration. For H_S = 5.0 kOe, a sharp and well defined maximum was present at x=0.27. The surprising result is that the K_u increases with increasing H_S for the entire Sm concentration. The increase is especially profound near the x for maximum K_u. This

behavior was not observed in field annealed alloys indicating that different formation mechanism is present in our films. The effective anisotropy field H_k was obtained by $H_k=2K_u/M_s$. The H_k as a function of x for different values of H_s is shown in figure 5.6.

Magnetic anisotropy constants can also be obtained by computing the area enclosed by initial M-H curves measured in directions perpendicular to film plane and in-plane parallel to easy axis. Since a large demagnetization field is present in thin films, the obtained perpendicular anisotropy constant K_p is the intrinsic anisotropy in the perpendicular direction and represents the energy required to rotate the magnetization from in-plane easy direction to normal to film plane direction.. If the film is homogeneous, the shape anisotropy energy density is $-2\pi M_s^2$. Then the effective anisotropy constant K_p^{eff} in perpendicular direction is

$$K_p^{eff} = K_p - 2\pi M_s^2$$

K_p^{eff} can not be determined by the above formula if the film is inhomogeneous. For the film shown in figure 5.2, K_p was $6.4X10^6$ erg/cm^3, the magnetostatic energy density $2\pi M_s^2$ was $3.1X10^6$ erg/cm^3, and the K_u was $3.3X10^6$ erg/cm^3, so that, within the accuracy of the measurement, the K_p^{eff} was the same as K_u. K_p was exclusively composed of K_u and $2\pi M_s^2$. This indicates that a true uniaxial anisotropy exists in the film with its easy axis in the film plane. But for general case, K_u and K_p^{eff} are not the same. K_p^{eff} can be either larger or smaller than the K_u. This behavior can not be covered by a single uniaxial anisotropy constant. The films should be biaxial and both K_u and K_p are necessary to characterize the magnetic anisotropy in the films. Figure 5.7 demonstrates this point. The sample in figure 5.7 was made at a substrate temperature of 550 K, in 100 mTorr gas pressure of Ar. The in-plane loops showed uniaxial behavior with a rectangular loop measured along in-plane easy direction and inclined loop measured

along in-plane hard direction. The K_u was $2.0X10^6$ erg/cm^3. The above mentioned point becomes evident from the loop measured in the direction perpendicular to the film plane. A large anisotropy field was present. The estimated K_p was $1.7X10^7$ erg/cm^3. Even accounting for the largest possible magnetostatic energy density $2\pi M_s^2$ of $3.0X10^6$ erg/cm^3, K_p^{eff} is still much larger than K_u. Another example of biaxial behavior is observed in samples that were annealed. In this case, the K_p^{eff} was negative which indicates the normal to plane direction was easy direction. However, in-the-film-plane anisotropy still existed. A more detailed discussion for this case will be given in later section.

A typical variation of K_p^{eff} with concentration is given in figure 5.8 for H_s=1.8 KOe. K_p^{eff} were plotted as a function of Sm concentration, x, by assuming that the film is homogeneous. In this case, K_p^{eff} was obtained from K_p and M_s by using the equation $K_p^{eff} = K_p - 2\pi M_s^2$. The dependence of the K_p on the H_s and concentration x were quite different from that of K_u as seen by comparing figure 5.5 and figure 5.8. K_p^{eff} was negative for low Sm concentration indicating that the easy axis was in the direction perpendicular to the film plane for these samples. It is questionable whether there is a true easy axis in the normal direction because the film may not be homogeneous so that the equation $K_p^{eff} = K_p - 2\pi M_s^2$ may not be valid. But some films did present an easy axis in perpendicular to film plane direction after annealing as discussed later on in this chapter. After switching signs around x=0.15, K_p^{eff} showed a broad maximum around x=0.27 and then decreased with the further increase of Sm concentration. Although K_p^{eff} and K_u showed the maxima around the same Sm concentration, their dependences on H_s vary from each other. K_p^{eff} was independent of H_s with Sm concentration dependence much stronger than that of K_u.

5.3.e. Coercive Field

The variation of room temperature intrinsic coercive force, $_iH_c$, measured in plane easy direction, with Sm concentration x is given in figure 5.9. This series of samples were made under the same conditions as that in figure 5.5 with H_s=3.0kOe. The effective anisotropy fields H_k are also plotted in the figure. $_iH_c$ increased smoothly in the range $0.1<x< 0.27$ and increased quite rapidly for $x>0.30$. A sharp maximum appeared for $x=0.35$. $_iH_c$ was at least a factor of 3 smaller than H_k and showed quite different trends from H_k. The maximum of H_k appeared at much smaller value of x than that of $_iH_c$. While the perfect rectangular in-plane hysteresis loop with no traces of magnetization rotation implied that the reversal merely took place by domain-wall motion, the relation between $_iH_c$ and H_k is unclear[53]. Figure 5.10 shows the variation of $_iH_c$ as a function of Sm content x for samples synthesized with H_s values of 1.8 and 3.0 kOe. They show similar trends for the range of x from 0.10 to 0.37 but the maximum value of $_iH_c$ is larger for film deposited at higher H_s.

5.3.f. Low Temperature Measurement

Low temperature magnetic measurements were performed for selected samples. Both intrinsic coercive force $_iH_c$ and in-plane anisotropy field K_u increased significantly at low temperatures. Figure 5.11 shows the demagnetization loop measured at 300 K(room temperature), 15K and 4.5k for sample composition $Sm_{20}Co_{80}$. The sample was grown at 100 mTorr Ar gas at room temperature at a rate of 2.0 Å/s and H_s of 3.0 kOe. The $_iH_c$ increased from 1.2 kOe at room temperature to 4.8 kOe at temperature of 4.5K. The initial M-H curves of the sample $Sm_{20}Co_{80}$ measured at 15K in direction of in-plane parallel and perpendicular to the easy axis are given in figure 5.12. The anisotropy field is

19 kOe at 15K compared to room temperature value of 5 kOe. The proportional increases of ${}_iH_c$ and K_u implies that the large value of ${}_iH_c$ at low temperature mainly resulted from the larger value of anisotropy field at low temperature.

5.3.g. Dependence of Magnetic Properties on T_{sub}

The substrate temperature, T_{sub}, plays an important role in the film growth process. At sufficiently high temperature, the adatoms have enough mobility to move along the film surface to equilibrium sites resulting in crystallization of the film. For SmCo films, the crystallization occurs at temperatures around 700 K. For samples synthesized at temperature below 700 K, only a broad diffraction peak was observed indicating the amorphous nature of the films.

If the temperature is sufficiently low, the adatoms do not have enough mobility to rearrange their positions and the resultant structures are determined solely by shading effects. Thus the K_u is expected to be small for films grown at sufficiently low temperature. Figure 5.13 shows the variation of K_u with the deposition temperature, T_{sub}, for sample $Sm_{20}Co_{80}$ with H_s=1.8kOe. K_u was much smaller for films grown at low temperature compared to those grown at room temperature.

In the intermediate range of the substrate temperature, the adatoms are expected to be able to adjust themselves locally to equilibrium positions, resulting in certain atomic scale structures. In-the-film-plane anisotropy K_u is the largest in this range of substrate temperature. From figure 5.13, it can be seen that the maximum of K_u appeared at somewhere around room temperature. K_u decreases with an increase in the T_{sub} when T_{sub} is above the room temperature. This trend is independent of the composition of the

samples as shown in figure 5.14 in which the variation of the K_u as a function of T_{sub} for samples with various Sm contents are given. The decrease of the K_u with T_{sub} can be explained by the pair ordering theory which will be discussed in a later section.

In contrast, a much stronger anisotropy was observed in films deposited at above ambient temperatures but below the crystallization temperature. This anisotropy has its easy axis in the film plane but with no preferred direction within that plane. More detailed discussion will be given in section 5.3.j.

5.3.h. Dependence of K_u on Pressure

It was found that K_u was a function of the pressure, P, of the sputtering gas as shown in Fig. 5.15. The samples in the figure had a Sm concentration of 23 at.% and were deposited at room temperature with an H_s of 3.0 kOe. K_u decreased quite rapidly with increasing pressure in the range $P < 50$ mTorr and then flattened out for higher pressures. This trend was independent of the composition of the samples.

5.3.i. Post Deposition Annealing

Post deposition annealing was performed for some samples. The samples were annealed in the temperature range 200 to 350 °C with field H_s being fixed in the same direction as during deposition. After 10 to 20 hours annealing, the in-plane anisotropy was greatly reduced, indicating that the thermal equilibrium pair distribution was different from that of the as deposited distribution. This suggested that the anisotropy induced in the growing surface layers become quenched by the accumulating film thickness. Subsequent field

annealing at elevated temperatures could then be expected to lower the degree of induced anisotropy by volume averaging the pair distributions. If the induced anisotropy formed during the deposition was three dimensional in nature, then field annealing at these relatively low temperatures would not be expected to lower the degree of anisotropy. In addition, lowering of the K_u on annealing, eliminates microcrystallinity as the source of anisotropy since the known crystalline phases of SmCo in our composition range are all very stable phases at these low annealing temperatures. Thus the origin of the anisotropy in our films was indicated to be surface induced short range ordering with a formation mechanism different from that of thermal annealing.

During annealing, the domains become aligned along the field direction so that anisotropic pair distribution can form throughout the sample volume. These relatively thick films act as bulk samples for thermal annealing. It is known that the thermal annealing is a relaxation process with the time constant strongly dependent on the temperature(54)(55). As long as the field is large enough to saturate the magnetization, it will have no effect on the pair distribution. Thus if H_S is greater than H_k in-plane then the anisotropy due to pair ordering is expected to be saturated. For our field induced films, the dependence of K_u on H_S implies that the pair distribution was affected by the magnitude of H_S. It should also be noted that the pair distribution in our films was formed during the film growth process. This differs from the anisotropy induced during field annealing, because the mobility of the atoms during the deposition was confined only to the surface of the growing film. The atoms below the surface were immobile since the substrate temperature was kept near room temperature. As the atoms arrived at the surface they diffused to energetically favorable sites on surface. At the surface, the temperature, and hence magnetization, was different from that inside the film. The H_S applied during the deposition process made some sites favor the formation of particular pair distributions.

This same distribution can not be obtained from the thermal annealing process because of the low mobility of the already deposited atoms in room temperature.

Post deposition annealing also revealed that the structure of the films synthesized at high and low sputter gas pressures were quite different. Annealing was performed in an in-plane magnetic field directed perpendicular to the direction of field applied during deposition. Figure 5.16 shows the hysteresis loops measured before and after post deposition annealing for the sample grown at a sputter gas pressure of 30 mTorr. A 12 hour annealing was performed at a temperature of 600 K. The plot on the left gives the loops measured before annealing in the direction of in-plane parallel to H_S, in-plane parallel to annealing field, and normal to film plane. The plot on the right gives loops measured in these directions after annealing. Obviously, the in-plane uniaxial anisotropy is still present in the sample, after the annealing, but with its easy axis reoriented along the direction of the annealing field. This process of easy axis reorientation is characteristic of field induced anisotropy in amorphous materials[54]. For film synthesized at 30 mTorr, K_u must be essentially due to a pseudodipolar anisotropy, which is attributed to the formation of a directional atomic pair ordering. It should be noted that the anisotropy was reduced after annealing. This can be explained by pair ordering theory in which the anisotropy decreases with increase in annealing temperature[55]. In our samples, the original anisotropy was formed at room temperature during deposition but the anisotropy after annealing was formed at an annealing temperature of 600 K. Figure 5.17 shows similar plots for a sample synthesized at a sputter gas pressure of 100 mTorr. The annealing was also performed at 600 K for 12 hours. After annealing, the original in-the-film-plane anisotropy was greatly suppressed but no other in-plane anisotropy could be introduced through the annealing process.

Further increase of the annealing temperature to 680 K leads to near total suppression of the in-the-film-plane anisotropy as shown in Fig. 5.18. After the in-the-film-plane anisotropy was suppressed, a perpendicular anisotropy was observed in the film with its easy axis normal to the film plane. This can be clearly seen after the shape anisotropy is corrected for in the hysteresis loop measured normal to the film plane as shown in Figure 5.18. The annealing was also performed at higher temperatures and for longer durations. No in-the-film-plane anisotropy was induced for annealing temperatures up to 700 K and for duration up to 24 hours. The samples became crystallized if annealed at temperatures higher than 725 K. The different annealing behavior of the samples grown at high and low gas pressures revealed their structural difference before annealing. For samples synthesized at high gas pressures, in addition to the formation of a directional atomic pair ordering, another growth induced structure developed during the growth process which favored the magnetization in the perpendicular direction. Different from the pair ordering, the growth induced structure was not affected by subsequent annealing. The fact that the growth induced structure was only developed in samples grown at high pressures revealed that the energy of the adatoms was the determining factor. The sputtering gas pressure basically determined the energy of the sputter atoms, or their effective temperatures, as they arrived at the substrate [7][38]. It has been shown that adatoms of Sm are not thermallized until the sputter gas pressure is around 100 mTorr of Ar. The formation of the growth induced structure obstructs the formation of the pair ordering. This can also be seen from the fact that K_u decreased as the pressure was increased.

5.3.j. Large Anisotropy with In-Plane Easy Direction

As mentioned before, a much stronger, third kind of anisotropy was observed in films deposited at above ambient temperatures. This third kind of anisotropy was evident from

a series of films made at various substrate temperatures, T_{sub}, at a gas pressure of 100 mTorr. With rise in T_{sub}, a steady rise in this anisotropy was observed. This anisotropy was similar to that observed in crystalline SmCo $TbCu_7$ type films, in that its easy axis was in the film plane but with no preferred direction within that plane[1][5]. The typical M-H loops can be seen in figure 5.7, in which the hysteresis loop measured along in plane hard and easy directions and perpendicular to the film plane direction are given. The variation of the anisotropy field, H_p, with the substrate temperature, T_{sub}, for sample $Sm_{22}Co_{78}$, is plotted in Fig. 5.19. The H_p was obtained by estimating the saturation field along the hard axis, which was the direction normal to the film plane. Figure 5.19 shows that H_p increased gradually with increase of T_{sub}. The samples grown at a substrate temperature of 570 K had a H_p of 34 kOe and were not fully crystallized. X-ray diffraction traces for a few values of T_{sub} are given in Fig. 5.20. The reflection peak corresponding to the strongest reflection of the major crystal structures of Sm-Co phase rapidly increased in intensity as T_{sub} was increased beyond 550 K. A corresponding rapid increase in H_p was observed as seen in Fig. 5.19. In contrast, in-the-film-plane anisotropy was observed to gradually decrease as T_{sub} increased. A theoretical model originally developed to explain the texture formed in crystalline films can be used to discuss the formation of this anisotropy. More details of this model are presented in the following section.

5.4. Magnetic Anisotropy in a-SmCo Films

In this section, in-the-film-plane anisotropy is explained by pair ordering model based on the theory developed by Neel to investigate the anisotropic bond orientations in ferromagnetic solid solutions(56). This theory is valid only in the intermediate range of the substrate temperature as we will explain later. As the substrate temperature is raised, a large anisotropy is formed with its easy direction in the film plane and dominated the growth process. A model has been developed by Prof. Cadieu to explain the anisotropy resulting from the textured crystallites in SmCo films. This model is adopted to explain the formation of this large anisotropy in amorphous films.

In above section we concluded that the origin of in-the-film-plane anisotropy in our films was surface induced short range ordering with a different formation mechanism from that of thermal annealing. Under the pair-model approximation, the formation of atomic structure are as following. First, the adatoms form bonds among themselves or with the preceding layer film atoms due to binding energy. This binding energy arises from pseudodipolar interactions discussed in chapter 2. Here we do not consider the much stronger nonmagnetic binding energy which is of the order of 10^{-11} erg/atom because of the fact that nonmagnetic binding energy is highly degenerate with respect to the atomic structure in amorphous materials. Then the bonds adjust their orientations to minimize the total magnetic energy. As we stated before, in the intermediate range of the substrate temperature, the adatoms are expected to be able to adjust themselves locally to equilibrium positions, resulting in certain atomic scale structures. However, if the substrate temperature is sufficiently high, the adatoms will have enough mobility to move in the surface to equilibrium sites in a larger scale resulting in crystallization of the film.

So only in the intermediate range of the substrate temperature, we can assume that the equilibrium orientations of the bonds obey the Boltzmann distribution. The probability of a bond oriented in (θ, φ) direction is:

$$p(\theta, \varphi) = A \exp[-w(\theta, \varphi)/k_B T_{sub}] \quad \text{----- (1)}$$

where k_B is Boltzmann constant and T_{sub} is the substrate temperature. w is bond energy which depends on the orientation of the bond and the spin of the two atoms. A is the normalization factor to make the total probability unity.

As the film grows, this distribution of bond orientations is expected to be retained in the film because the mobility of the atoms during the deposition is confined only to the surface of the growing film. This distribution can lead to in-the-film-plane anisotropy observed in our films. Similar approach has been used for modeling the directional ordering of solid solutions or induced magnetic anisotropy(57)(58).

We describe the bulk anisotropy energy density as a sum of energies of the bond between two atoms (the pair-model approximation). Considering only the pseudodipolar interaction term in bond energy, the anisotropy energy density by a particular bond is given by

$$w(\cos\theta_b) = I(T)(\cos^2(\theta_b)-1/3) \quad \text{------(2)}$$

where $I(T)$ is the pseudodipolar interaction constant at temperature T, and θ_b is the angle between magnetic moment and bond direction.

Further calculation needs a specific coordinate system. In the spherical coordinate system defined in figure 5.21, Z and X axes are in the film plane and Y axis is in the normal direction. We also put Z axis in the H_S direction which is the direction of magnetization of the films. When adatoms couple with atoms on the surface, their spin will be in the Z direction (parallel or antiparallel). Thus the energy of a bond in direction (θ, φ) will be

$w(\theta, \varphi)=w(\cos\theta_b)=l(T_{sub})(\cos^2\theta - 1/3)$ ------(3)

As we state above, the probability of a bond oriented in (θ, φ) direction in a film deposited with H_S present follows the Boltzmann distribution $p(\theta, \varphi)$. The Boltzmann distribution of bond orientations is build up during the film growth.

When an external field is applied in the film plane other than the easy direction(Z axis), the magnetization is in the direction of (θ_m, 0). The bulk anisotropy energy density will be

$$E_a = N \int_0^{2\pi} \int_0^{\pi} w'(\cos\theta_{mb})\, p(\theta,\phi) \sin\theta \, d\theta d\phi$$

------(4)

where, N is the density of the bonds involved and, θ_{mb}, the angle between the magnetization and bond orientation, is given by

$\cos\theta_{mb} = \sin\theta_m\sin\theta\cos\varphi + \cos\theta_m\cos\theta$ ------(5)

Note that w' refers to the bond energy at the magnetic measurement temperature, which is room temperature, T_{room}. Substituting Eq. (1), (3) and (5) into Eq. (4), the energy density can be expanded as

$$E_a(\theta_m) = K_0 + K_1\sin^2\theta_m + K_2\sin^4\theta_m + \ldots \quad \text{------(6)}$$

Considering that the bond energy (10^{-15}erg) is much smaller than k_BT_{sub} ($4X10^{-14}$erg for T_{sub}=300K), Eq. (1) can be simplified as

$$p(\theta, \varphi) = 1/4\pi[1 - w(\cos\theta)/k_BT_{sub}] \quad \text{-----(7)}$$

Assuming the bond energy contains mainly the dipolar term, then

$$w(\cos\theta) = l(T_{sub})(\cos^2\theta - 1/3)$$

and

$$w'(\cos\theta_{mb}) = l(T_{room})(\cos^2\theta_{mb} - 1/3)$$

Eq (4) can be analytically calculated. Note that the terms with odd powers of $\cos\varphi$ vanish after integration over φ. K_1 is obtained as

$$K_1 = 2N\, l(T_{room})\, l(T_{sub}) / 15k_BT_{sub} \quad \text{------(8)}$$

To compare with experimental value of K_u, we consider the Sm_xCo_{1-x} film. The in-plane anisotropy is mainly contributed by Sm-Co bonds. The Sm-Co bond density N_b depends

on the concentrations of Sm and Co atoms and is given by N = nx(1-x)Z, where n is total atomic density and Z is the average coordination number.

Assume x=0.2, Z=12, $n=8X10^{22}cm^{-3}$, $T_{room}=T_{sub}=300K$ and $l=10^{-15}erg$, uniaxial anisotropy K_1 given by equation (8) is 10^6 erg/cm^3. So the Boltzmann distribution of the bonds does give the correct order of magnitude of in-plane anisotropy. Note that only a small anisotropy in the pair distribution is enough to explain the magnetic anisotropy of a-RE-TM alloys(59).

To evaluate the variation of K_1 with concentration x and temperature, we need to evaluate the variation of $l(T)$ with x and T. Following the approach given by ref(57), a reasonable estimate is based on the pseudodipolar model of the interaction. The energy is written in the form

$$H_d = \Sigma A_{pq}^{ij} S_p^i S_q^j$$

where S_p^i is the q^{th} Cartesian component of the spin on the i^{th} point, and A_{pq}^{ij} are the coefficient constants of the pseudodipolar interaction. If correlation between spin orientations are neglected, the quantity S_p^i may be replaced by its thermal average. In ferromagnetic materials this average would be proportional to the spontaneous magnetization M(T). It follows that l(T) is the thermal average of H_d and so proportional to $M^2(T)$.

Then it follows that

$$K_u = Af(x)*(Ms(T_{room})/Ms(0))^2*(Ms(T_{sub})/Ms(0))^2$$

where $f(x) = x^2(1-x)^2$, $M(T_{room})$, $M(T_{sub})$ and $M(0)$ are the saturation magnetizations at room temperature, the deposition temperature, and 0 K respectively. $M(T)/M(0)$ was assumed to be given by Weiss mean field theory as $y = \tanh(y/a)$, where $y = M(T)/M(0)$ and $a = T/T_c$, where T_c is the Curie temperature. Only limited data are available for the dependence of T_c on the Sm concentration in a-SmCo. For $0.40 < x < 0.60$, we use the data from previously published works [52] and for lower Sm concentrations, we assume the T_c of the amorphous phases to be the same as their crystalline counterparts. The dependence of T_c on x was then interpolated for the range of $0.10 < x < 0.40$. Thus the expected values of K_u can be evaluated as a function of x. The result is shown in Fig. 5.22. In the same figure, the experimental data for $H_s = 3.0$ kOe are also plotted. As can be seen in the figure, the experimental data agree well with the expected dependence of K_u on the Sm concentration.

As already discussed in previous section, a large anisotropy was observed to gradually develop in the film with its easy axis in the film plane but with no preferred direction in the film plane for films deposited at increasing T_{sub}. The same kind of anisotropy has also been also observed in crystalline SmCo films with the $TbCu_7$, Th_2Zn_{17}, or $CaCu_5$ type structure. In these cases, the pair ordering theory is inadequate.

A theoretical model has been proposed by professor Cadieu to explain the texture in directly crystallized films of uniaxial materials[1]. Following that model, for those systems that are grown at temperature below Curie temperature, the demagnetization energy should favor the growth of the domains with the easy directions of magnetization in the film plane. The demagnetization energy at the deposition temperature is

$$E_d = -2\pi(M_s(T_{sub}))^2 V\cos^2(\theta),$$

where θ is the angle between the easy axes of magnetization and the substrate plane. The demagnetization energy must exceed $k_B T_{sub}$ if the demagnetization energy is to be expected to influence preferential alignment of the easy axes of the magnetization of the crystallites.

5.5. Conclusions

With a large H_S present, a well defined and large in-the-film-plane magnetic anisotropy of exceptionally high value of $K_u = 3.3 \cdot 10^6$ erg/cm^3 has been obtained in amorphous SmCo films. This is the largest value ever reported for in-the-film-plane anisotropy induced during the film deposition process. The in-plane anisotropy K_u depended essentially on the applied field H_S and Sm concentration. For $H_S = 5.0$ kOe the in-plane hard axis loop became closed and the in-plane easy axis loop parallel to the H_S direction became rectangular. For $H_S = 5.0$ kOe, the value of K_u and K_p^{eff} became equal at $x = 0.27 \pm 0.02$. This indicated that there was a true uniaxial anisotropy for the high H_S value at the composition. The pseudodipolar pair ordering theory can explain fairly well the dependence of K_u on the Sm concentration. We concluded that surface induced short range ordering was the origin of in-the-film-plane anisotropy observed in amorphous films deposited in a magnetic field. The formation mechanism is different from that of the short range ordering induced by field annealing. We have found that both in-the-film-plane, and perpendicular, anisotropy can be present in sputter synthesized amorphous SmCo films depending on the film preparation conditions. Different sources of anisotropy can be distinguished in these films. The physical origin of in-the-film-plane anisotropy was explained as directional pair ordering. The perpendicular anisotropy was only formed in films synthesized through thermallized sputtering and can not be explained by directional pair ordering. A large anisotropy was observed in films deposited at above ambient temperatures, with its easy axis in the film plane but without any preferred direction in the film plane. Both the formation of growth induced structure which caused the perpendicular anisotropy, and the formation of a third type of anisotropy, prevented the formation of the pair ordering, and decreased the in-the-film-plane anisotropy.

CHAPTER 6. THIN SmCo FILMS

6.1. Introduction

In several micromagnetic applications, magnetic bias field supplied by thin films are necessary(60)(61). The Rare Earth- Transition Metal (RE-TM) permanent film magnets have showed extreme anisotropy, coercivity and energy products, which depend on uniaxial magnetocrystalline anisotropy arising from the single ion anisotropy of the Rare Earth atoms (3). It can provide large and more uniform biasing fields compared to conventional magnetic materials. Textured films of RE-TM materials have been successfully sputter synthesized on polycrystalline substrates with thickness of several microns (6)(5). In this chapter, synthesis of anisotropic Sm-Co films of thickness ranging from several hundred to several thousand angstroms are reported. Study of grain size and magnetic property dependence on the film thickness was carried out, for film thickness ranging from 500 Å to several microns.

6.2. Results and Discussion

The Sm-Co films were directly crystallized at a composition range where the crystal structure is of the disordered 1-5 or $TbCu_7$ type structure. The Sm-Co permanent magnet films have composition of $Sm_{14.4}Co_{56.8}Fe_{19.5}Cu_{7.6}Zr_{1.7}$ and are directly crystallized on substrates at 350 °C from commercially available TDK targets by sputtering at 60 mTorr Ar pressure. For all the films in this study, to ensure film purity, prior to deposition a substrate mask was used while sputter etching the target surface.

The hysteresis loops of the Sm-Co permanent magnets of various thickness are given in figure 6.1. All the loops are measured in the film plane. Even at thickness of 500Å, the shape of the hysteresis loop is still near rectangular. But it is clear that the coercivity and loop squareness improve with the increase of film thickness. At thickness of 1800Å, both the coercivity and loop squareness are already very close to that of films of several microns thick. In Fig. 6.2, the scanning electron microscope (SEM) image of the film surfaces for two thicknesses are given. It indicated that the grain size in the film increases with film thickness. Dependence of average grain size on the film thickness is given in Fig. 6.3. The similar trend of variation of coercivity and grain size with thickness indicates that the grain size is the key factor in determining the coercivity and loop squareness in SmCo thin films. X-Ray diffraction of the thicker films synthesized under similar conditions indicated a total alignment of the crystallite c-axis in the film plane. However, magnetic measurements indicated no preferred c-axis orientation within the film plane. The similar magnetic properties among films with various thickness indicate that they have the similar texture distribution. Since the polycrystalline substrates are used, surface and interface energy minimization during grain growth can lead to films composed of grains with

texture but with no preferred in plane orientation. On polycrystalline substrates, there is no interface energy anisotropy for grain rotations in the film plane. Nonepitaxial growth mode are the character in our films. The low hysteresis loop squareness of the 500 Å thick film compared to those of the thicker films also indicated that in this nonepitaxial growth mode of the film, the initial layers contained crystallites with less degree of texture. As the film grew thicker, crystallites of certain orientations became the dominant growth mode and eventually result in highly textured grains.

To explain the coercive force mechanism in these films, initial magnetization curves were measured. In SmCo materials, two mechanisms, nucleation and pinning, are involved. In essentially single phase magnets of $SmCo_5$, nucleation is the dominant mechanism. In this case, the grain boundaries are effective in prohibiting domain wall displacement. The magnetization reversal is through the nucleation of reversed domains at the walls and their subsequent rapid growth. The initial magnetization curves for this case are characterized by the rapid saturation in low field as shown in figure 6.4. The pinning is the basic mechanism of coercive force in 2-17 alloys with composition $Sm_2(Co,M)_{17}$, M being a combination of transition metals. In this material, the developed microstructures provide a network of pinning sites for domain walls within the grain interiors. ${}_iH_c$ is then the field strength at which the wall are released so that a reversal can take place through wall displacement. The initial magnetization curves then are characterized by a very low magnetization until the applied field has reached the level of coercive force as shown in figure 6.4.

The initial curve for our film is also shown in figure 6.4. It is not dominated by pinning mechanism as in bulk 2-17 material. Instead, a mixture of two type of mechanism is seen. It is reasonable since our films were of single phase $TbCu_7$ type. There is no other boundary phase present in the film. Our films are insensitive to the heat treatment, which

is as expected, since the developed microstructures are not essentially important in our films.

CHAPTER 7 MODULATED MULTILAYER FILMS

7.1. Introduction

The successful synthesis of Sm-Co type film magnets that exhibit large in plane energy products made it possible to synthesize modulated multilayer permanent magnet films. Multilayered permanent magnet films can now be sputter synthesized such that, while each individual layers exhibited high in-plane static energy products, the alternating layers differed in their coercive force[62]. After this layered system is saturated in-plane, a reversed field of intermediate value can be used to reverse the magnetization of only low coercivity layers. Upon removal of the external field, the in-plane magnetizations are oppositely directed in successive layers. The thickness of the composite system then constitutes a fine-scale periodic permanent magnet array. Such an array becomes useful as an undulator structure when the periodically reversing magnetic field from successive layers is used to alternately deflect an electron beam.

To retain the high energy product for each layer in this state, besides having a large difference of coercivity between alternating layers, it is necessary for each layer to be synthesized with c-axes aligned in the film plane, so that each layer has a square shaped hysteresis loop. A sputter deposition method has been developed that allows the synthesis

of Sm-Co type film magnets exhibiting an in plane energy product in the 20MGOe range. The method allows modification of film composition, magnetic properties, and crystal structure through a process control involving deposition temperatures, sputter gas species, and pressures[5][63][64]. This method was used here to synthesize modulated multilayer permanent magnet films.

7.2. Results and Discussion

The investigated films were synthesized through sputter deposition onto polished Al_2O_3 substrates from commercially available Sm-Co based TDK bulk magnet targets. Thickness of the films vary from 800 Å to above 10 μm, and the number of layers in the films ranged from two to ten. During sputtering, the differences in the atomic masses, collision cross section, and vapor pressures of Sm atoms versus TM atoms can be used to vary the film Sm content from 12 at.% to 18 at.% by varying the sputtering parameters from the same targets. Thus through process control, the layered system was synthesized without changing either the targets or substrate location.

Two types of layered structures have been synthesized. In the first type, alternating layers of directly crystallized rhombohedral phase and subsequently crystallized $TbCu_7$ phase have been used. In the other type, alternating layers of directly and subsequently crystallized $TbCu_7$ phase have been used. The best results were obtained from second type layered films as explained later. The following discussion will be concentrated on results from second type layered films.

The layers showing relatively low coercive force of around 4-6 kOe were synthesized through direct crystallization by depositing the film on heated substrate of 400-500 °C in gas pressures around 55 mTorr. The layers showing relatively higher coercive forces of 12-16 kOe were synthesized through subsequent crystallization by first carrying out the sputter deposition at gas pressures around 65 mTorr with substrates cooled to room temperature and then subsequently heating the substrates to 450-550 °C to cause crystallization. These steps can be repeated for successive sets of layers since it is only the

initial heating that affects the properties, particularly for $TbCu_7$ type layers. The processing differences for the two types of layers in term of deposition temperatures and gas pressures caused the directly crystallized layers to be relatively Sm poorer. The composition of the individual directly and subsequently crystallized film layers are $Sm(TM)_{5.90}$ and $Sm(TM)_{5.45}$ respectively, as against the target composition of $Sm(Co_{0.66}Fe_{0.23}Cu_{0.09}Zr_{0.02})_{6.09}$. The relative ratios of the various transition-metal atoms are about the same as in target. The subsequently crystallized layers are made of grains of diameter around 600 Å as shown in figure 7.1 in which the micrograph obtained from scanning electron microscope are given. Also, in subsequently crystallized layers, magnetic anisotropy is higher than that of directly crystallized layers as a result of the higher Sm concentration. Both factors cause the coercive forces for these subsequently crystallized layers to be as high as 13-16 kOe. On the other hand, the directly crystallized layers show weak columnar structures and larger grain size as shown in figure 7.2 in which SEM mircograph of the cross section of a two layered film is given. For these layers, reduced Sm concentration and the larger grain size both contribute to a lower coercivity in the 4-6 kOe range.

In figure 7.3, the hysteresis loops of individual directly and subsequently crystallized $TbCu_7$ type films are given. The magnetic properties of individual directly and subsequently crystallized layers in multilayered film should be the same as that in figure 7.3 (a) and (b) respectively, assuming the coupling between layers is insignificant. The hypothetical hysteresis loop of a multilayered film such as in figure 7.3 (a) and (b) is also given.

In figure 7.4, a hysteresis loop for a multilayered film such as shown in figure 7.2 is given. For this film, the interlayer transition region width is small compared to the layer thickness as seen from the SEM micrograph in figure 7.2. For such layered films, the $4\pi M$ values

are simply a relative-thickness-weighted sum of the magnetizations of the separate layers. It should be noted that there is a striking similarity between the hysteresis loop of the multilayered film of figure 7.4 and the hypothetical loop of figure 7.3(c) which is the weighted sum of the magnetization of individual films in figure 7.3(a) and (b). The drop in second quadrant of the hysteresis loop of multilayered film in figure 7.4 corresponds to the reversal of the magnetization in layers with lower coercive force. The drop in third quadrant corresponds to the reversal of the magnetization in the layers with higher coercive force. The individual layer characteristic is very clear in this layered film. However, as the layer thickness is lowered to be around 800 Å, which is only slightly larger than the 600 Å grain size observed for subsequently crystallized films, the differences in magnetic properties of the layers become less distinguishable.

In the ideal case for flat-topped rectangular hysteresis loops, after saturating the multilayered film in one direction, the field could be reversed to an intermediate value to reverse only the low-coercivity layers. The net magnetization would then be zero even through the individual layers would have oppositely directed magnetization with maximum magnetic energy densities. In actual practice, hysteresis loops are not flat topped, but have a positive slope for the major loop on the $+4\pi M$ axis at $H=0$[65]. To retain the high energy product for each layer in this state, besides having a large difference of coercive force between alternating layer, it is necessary for each layer to be synthesized with c-axes aligned in the film plane, so each layer has a square shape hysteresis loop. The fact that the layers have different coercivities allows a large partial extent reversed magnetic field to be applied such that the remanent moments of the low-coercivity layers are reversed without appreciably demagnetizing the high-coercivity layers. It is desirable to quantify the amount of magnetic energy density that can be established in this system, after exposure to a partial demagnetizing field. The total energy density of the modulated film

layers will then be a function of the reverse-field value and of the shape of the individual hysteresis loops.

For a hysteresis loop with finite slope at H = 0, it can be shown that the maximum energy product is

$$BH_{max} = [(4\pi M_r)^2/4](1+\mu_{RP})^{-1}$$

where $4\pi M_r$ is the remanent induction and μ_{RP} is the reversible permeability which is the slope for major loop on the $+4\pi M$ axis at H=0. For noncoercivity-limited minor loops, it can also be shown that if a system is partially demagnetized so that it recoils to a minor loop remanence of $4\pi M_{rc}$, the maximum energy product from that point is

$$(BH_{max}) = [(4\pi M_{rc})^2/4](1+\mu_{RP})^{-1},$$

where μ_{RPm} is the reversible permeability of the minor loop. Please note that $4\pi M_{rc}$ is a function of the reverse field.

The ratio of the maximum energy product after being explored to some demagnetizing field to that of major loop can be used as a figure of merit. We have defined a reversed-energy-density (RED) figure of merit for the multilayer film as

$$RED(H) = 1/2|(M_{rc1}/M_{r1})^2 - v(M_{rc2}/M_{r2})^2|,$$

where the subscripts 1 and 2 refer to the higher-coercivity and lower-coercivity layers. The factor v=1 if the layers are magnetized in the same direction, and v=-1 if the layers are magnetization in opposite direction. H is the reverse field. For simplicity, the μ_{RP} values

for the different types of layers have been assumed to be equal so as to cancel out the factor. The value of reversed-energy-density (RED) varies from 0 to 1. In general, RED value is a function of reverse field and reaches maximum value for some intermediate value of applied reverse field. The maximum value of RED is sensitive to the different hysteresis loop shapes characteristic of different types of materials and can be used as a measure of magnetic energy density being retained in the layered system. The maximum RED value of 1 can only be reached when the hysteresis loops of both types of layers are truly flat topped. In this case, both types of layers can retain their maximum energy products. The value of RED is 0 if both types of layers are magnetized in the same direction.

In figure 7.5, the RED values for layered film shown in figure 7.2 and 7.4 as a function of reverse field are given. The minor loop remanent $4\pi M_{rc}$ which is estimated as $4\pi M_{rc}=4\pi M_H(1-\mu_{RP}H)$ is also given. The maximum RED for this film is 0.86 as seen from figure 7.5. The maximum RED value of 0.9 have been measured for directly and subsequently crystallized $TbCu_7$ type layered films. In contrast, rhombohedral and $TbCu_7$ layered films have only been made with maximum RED value of 0.76 for the order of micrometer-thick layers. The reversed-energy-density (RED) value is thus useful for quantifying the magnetic energy density that can be retained for different types of multilayer system.

CHAPTER 8 CONCLUSIONS

A systematic study of the deposition processes and magnetic properties for the Sm-Co film system has been carried out. Films of Sm-Co system with various magnetic anisotropies have been synthesized through sputter deposition in both crystalline and amorphous phases. The origins of various anisotropies have been studied.

Thermallized sputter deposition process control was used to synthesize Fe enriched Sm-Co based films with rhombohedral 2-17 Th_2Zn_{17} type structure. The rhombohedral 2-17 crystallites exhibited unusually strong textures with their crystallographic c axes in the film plane resulting in a large anisotropy with its easy axis in the film plane. The saturation magnetization of Fe enriched films was substantially higher than that of non-enriched films. The energy products of the Fe enriched films were in the 19-20 MGOe range after post deposition heat treatment. Unusually strong (220) texturing was present in the Fe enriched 2-17 films, even in the absence of total alignment of c axes in the film plane.

A set of crystalline films with thicknesses ranging from several hundred to several thousand angstroms were synthesized to investigate the early stages of grain growth and the corresponding magnetic properties. Even at thickness of 500Å, the shape of hysteresis loop is still near rectangular. Magnetic measurements indicated an alignment of the crystallite c-axis in the film plane but no preferred c-axis orientation within the film plane. The similarities in the variations of coercivity and grain size with thickness indicated that the grain size is the key factor in determining the coercivity and loop squareness in SmCo thin film.

When film deposition temperature was below crystallization temperature, several types of anisotropies were formed in the films. A large in-the-film-plane anisotropy could be induced in the SmCo films by applying a magnetic field in the film plane during deposition when the substrate temperature was below the crystallization temperature. With a large H_S present, a well defined and large in-the-film-plane magnetic anisotropy of exceptionally high value of $K_u = 3.3 \times 10^6$ erg/cm^3 has been obtained in amorphous SmCo films. This is the largest value ever reported for in-the-film-plane anisotropy induced during the deposition process. For films with well defined in-the-film-plane anisotropy, the loop measured along in-plane hard axis had an undetectable opening and the loop along in-plane easy axis was a perfect rectangular. It was found that the in-the-film-plane anisotropy K_u depended essentially on the applied field H_S and Sm concentration. The variation of K_u with Sm concentration presents a well defined maximum for $H_S > 1.8$ kOe. The maximum values of K_u increases with the increasing of H_S. The pseudodipolar pair ordering theory can explain fairly well the dependence of K_u on the Sm concentration.

It was found that both in-the-film-plane and perpendicular anisotropy can be present in sputter synthesized amorphous SmCo films depending on the film preparation conditions. For films synthesized at a sputter gas pressure of 30 mTorr, only in-the-film-plane anisotropy was present and the easy axis was reoriented to the direction of annealing field after post deposition annealing. In contrast, both in-the-film-plane and perpendicular anisotropy appeared in films synthesized through thermallized sputtering at a sputter gas pressure of 100 mTorr and the in-plane easy axes of these films could not be reoriented through post deposition annealing. A large anisotropy was observed in films deposited above ambient temperatures, with easy axis in the film plane but without preferred direction within the film plane. Since the films were in amorphous phase, the crystalline anisotropy was not the origin of this anisotropy.

It was concluded that surface induced short range ordering was the origin of in-the-film-plane anisotropy observed in amorphous films deposited in the presence of a magnetic field. The formation mechanism was different from that of the short range ordering induced by field annealing. The perpendicular anisotropy was shown to be growth induced and only formed in films synthesized through thermallized sputtering and could not be explained by directional pair ordering. Both the formation of growth induced structure which caused the perpendicular anisotropy, and the formation of a third type anisotropy, prevented the formation of the pair ordering, and decreased in-the-film-plane anisotropy.

Multilayered films have been sputter synthesized through modulation of film growth. In these modulated multilayer films, alternating layers could be synthesized through modulation of composition and texture. The successful synthesis of Sm-Co type film magnets that exhibit large in plane energy product and wide range of coercivity made it possible to synthesize modulated multilayer permanent magnet films. Multilayered permanent magnet films can be sputter synthesized such that, while each individual layers exhibited high in-plane static energy products, the alternating layers differed in their coercive force. The fact that the layers have different coercivities allowed a large partial extent reversed magnetic field to be applied such that the remanent moments of the low-coercivity layers are reversed without appreciably demagnetizing the high-coercivity layers. A method has been developed to quantify the amount of magnetic energy density that can be established in this system, after exposure to a partial demagnetizing field.

Compound	Lattice Constants (Å)	Crystal symmetry	Structure type
Sm_3Co	a=7.090 b=9.625 c=6.342	orthorhombic	Fe_3C
Sm_9Co_4	a=11.15 b=9.461 c=9.173	orthorhombic	unknown
$SmCo_2$	a=7.260	cubic	$MgCu_2$
$SmCo_3$	a=5.050 c=24.590	rhombohedral	$GdCo_3$
Sm_2Co_7	a=5.041 c=24.327	hexagonal	Ce_2Ni_7
$SmCo_5$	a=5.002 c=3.964	hexagonal	$CaCu_5$
Sm_2Co_{17}	a=8.395 c=12.216	rhombohedral	Th_2Zn_{17}
Sm_2Co_{17}	a=8.360 c=8.515	hexagonal	Th_2Ni_{17}

Table 2.1

6(c), $(0, 0, \frac{1}{3})$, $(\frac{1}{3}, \frac{2}{3}, 0)$, $(\frac{2}{3}, \frac{1}{3}, \frac{2}{3})$

$(0, 0, \frac{2}{3})$, $(\frac{1}{3}, \frac{2}{3}, \frac{1}{3})$, $(\frac{2}{3}, \frac{1}{3}, 0)$

9(d), $(\frac{1}{2}, 0, \frac{1}{2})$, $(0, \frac{1}{2}, \frac{1}{2})$, $(\frac{1}{2}, \frac{1}{2}, \frac{1}{2})$

$(\frac{5}{6}, \frac{2}{3}, \frac{1}{6})$, $(\frac{1}{3}, \frac{1}{6}, \frac{1}{6})$, $(\frac{5}{6}, \frac{1}{6}, \frac{1}{6})$

$(\frac{1}{6}, \frac{1}{3}, \frac{5}{6})$, $(\frac{2}{3}, \frac{5}{6}, \frac{5}{6})$, $(\frac{1}{6}, \frac{5}{6}, \frac{5}{6})$

18(f), $(\frac{1}{3}, 0, 0)$, $(0, \frac{1}{3}, 0)$, $(\frac{2}{3}, \frac{2}{3}, 0)$

$(\frac{2}{3}, 0, 0)$, $(0, \frac{2}{3}, 0)$, $(\frac{2}{3}, \frac{2}{3}, \frac{2}{3})$

$(\frac{1}{3}, \frac{1}{3}, 0)$, $(\frac{1}{3}, 0, \frac{2}{3})$, $(0, \frac{1}{3}, \frac{2}{3})$

$(0, \frac{2}{3}, \frac{2}{3})$, $(\frac{1}{3}, \frac{1}{3}, \frac{2}{3})$, $(\frac{2}{3}, 0, \frac{2}{3})$

$(0, \frac{1}{3}, \frac{1}{3})$, $(\frac{2}{3}, \frac{2}{3}, \frac{1}{3})$, $(\frac{1}{3}, 0, \frac{1}{3})$

$(\frac{1}{3}, \frac{1}{3}, \frac{1}{3})$, $(\frac{2}{3}, 0, \frac{1}{3})$, $(0, \frac{2}{3}, \frac{1}{3})$

18(h), $(\frac{1}{2}, \frac{1}{2}, \frac{1}{6})$, $(\frac{1}{2}, 0, \frac{1}{6})$, $(0, \frac{1}{2}, \frac{1}{6})$

$(\frac{1}{2}, \frac{1}{2}, \frac{5}{6})$, $(\frac{1}{2}, 0, \frac{5}{6})$, $(0, \frac{1}{2}, \frac{5}{6})$

$(\frac{5}{6}, \frac{1}{2}, \frac{5}{6})$, $(\frac{5}{6}, \frac{2}{3}, \frac{5}{6})$, $(\frac{1}{3}, \frac{1}{6}, \frac{5}{6})$

$(\frac{5}{6}, \frac{1}{6}, \frac{1}{2})$, $(\frac{5}{6}, \frac{2}{3}, \frac{1}{2})$, $(\frac{1}{3}, \frac{1}{6}, \frac{1}{2})$

$(\frac{1}{6}, \frac{5}{6}, \frac{1}{2})$, $(\frac{1}{6}, \frac{1}{3}, \frac{1}{2})$, $(\frac{2}{3}, \frac{5}{6}, \frac{1}{2})$

$(\frac{1}{6}, \frac{5}{6}, \frac{1}{6})$, $(\frac{1}{6}, \frac{1}{3}, \frac{1}{6})$, $(\frac{2}{3}, \frac{5}{6}, \frac{1}{6})$

6(c), $(0, 0, 0.097)$, $(0, 0, -0.097)$ $(\frac{1}{3}, \frac{2}{3}, \frac{2}{3}+0.097)$

$(\frac{1}{3}, \frac{2}{3}, \frac{2}{3}-0.097)$, $(\frac{2}{3}, \frac{1}{3}, \frac{1}{3}+0.097)$,

$(\frac{2}{3}, \frac{1}{3}, \frac{1}{3}-0.097)$

Table 2.2

Powder Diffraction Pattern of

Sm_2Co_{17} (HEXAGONAL) Th_2Ni_{17} Type

d(a)	Intensity	hkl
3.329	20	201
2.928	50	112
2.420	55	300
2.092	80	220
2.081	100	302
2.044	45	004
1.933	20	213
1.864	50	223
1.561	20	304
1.476	40	412
1.462	40	224
1.396	30	330
1.321	35	332
1.209	45	600

Table 4.1

Powder Diffraction Pattern of

Sm_2Co_{17} (Rhombohedral) Th_2Zn_{17} Type

d(a)	Intensity	hkl
2.916	50	113
2.803	20	104
2.425	60	300
2.317	50	024
2.098	100	220
2.081	100	303
2.041	40	214
2.025	20	006
1.866	60	223
1.825	50	116,125
1.680	20	134
1.555	40	306,315
1.477	40	143
1.466	40	217,324
1.457	60	226,045
1.401	40	330
1.376	20	235
1.322	100	333
1.313	40	137,054
1.290	40	119
1.255	40	407,244
1.212	100	600

Table 4.2

Powder Diffraction Pattern of Sm_2Co_{17} (DISORDERED) $TbCu_7$ Type		
d(a)	Intensity	hkl
2.929	30	101
2.428	30	110
2.103	45	200
2.087	100	111
2.041	30	002
1.869	20	201
1.481	12	211
1.464	20	202

Powder Diffraction Pattern of $SmCo_5$ (HEXAGONAL) $CaCu_5$ Type		
d(a)	Intensity	hkl
2.926	70	101
2.498	54	110
2.163	54	200
2.115	100	111
1.988	19	002
1.900	16	201
1.513	15	211
1.464	20	202
1.354	21	301
1.248	20	220

Table 4.3

$TbCu_7$	Th_2Zn_{17}	Th_2Ni_{17}
	202	
101	113	112
	104	203
	211	211
	122	103
110	300	300
	024,015	212
		203
200	220	220
111	303	302
	214	
002	006	004
	312	213
201	223	222
102	116	114
	042	401
	107	321
	134	410
	232	
	027, 404	
112	306	304
211	143	412
	217, 324	
202	226	224
		323
300	330	330
	235	006
	422	
301	333	332

Table 4.4

2θ		INDEX	
	TH_2NI_{17} A=8.482 C=8.118	TH_2ZN_{17} A=8.482 C=12.177	$TBCU_7$ A=4.897 C=4.059
28.45		202	
30.36	112	113	101
37.05	300	300	110
42.98	220	220	200

Table 4.5

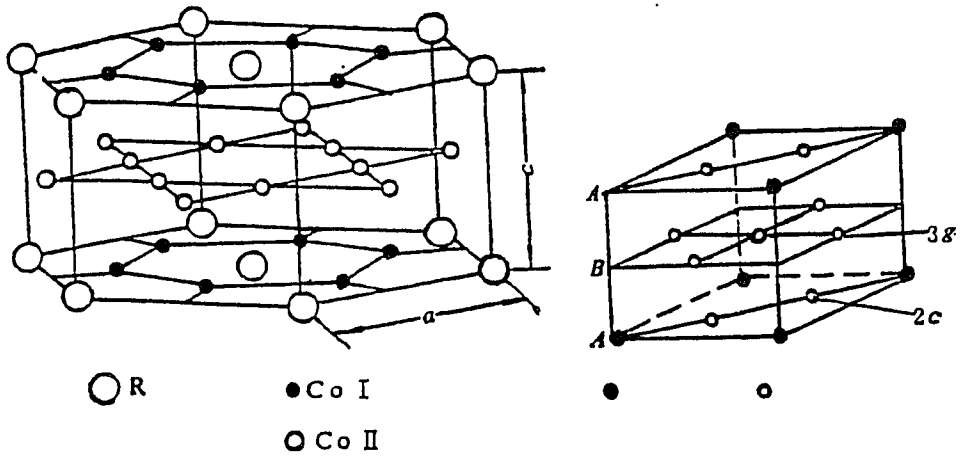

Figure 2.1

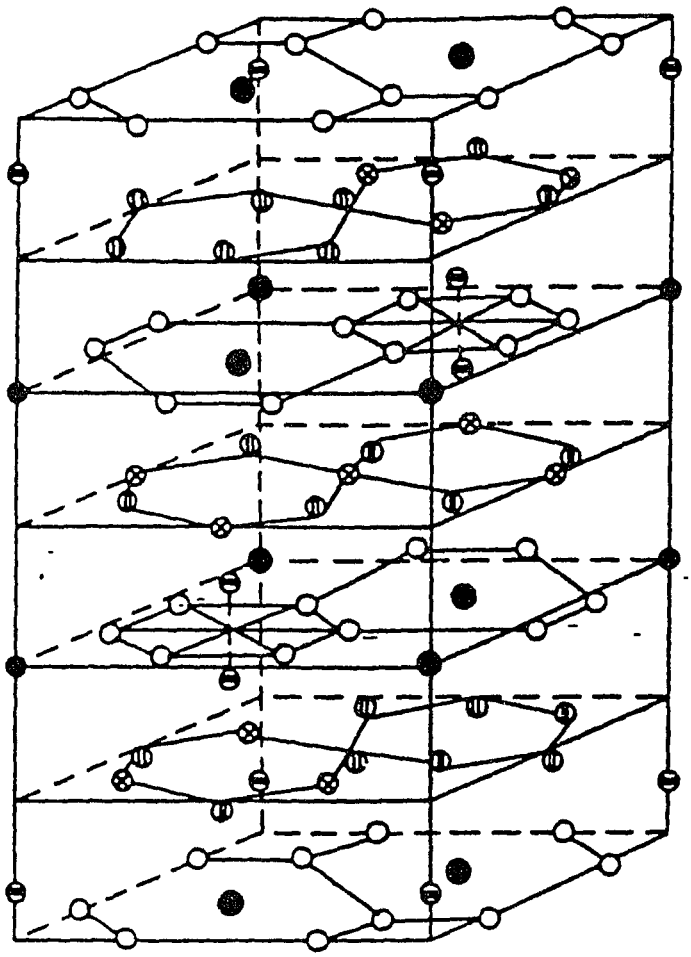

Figure 2.2

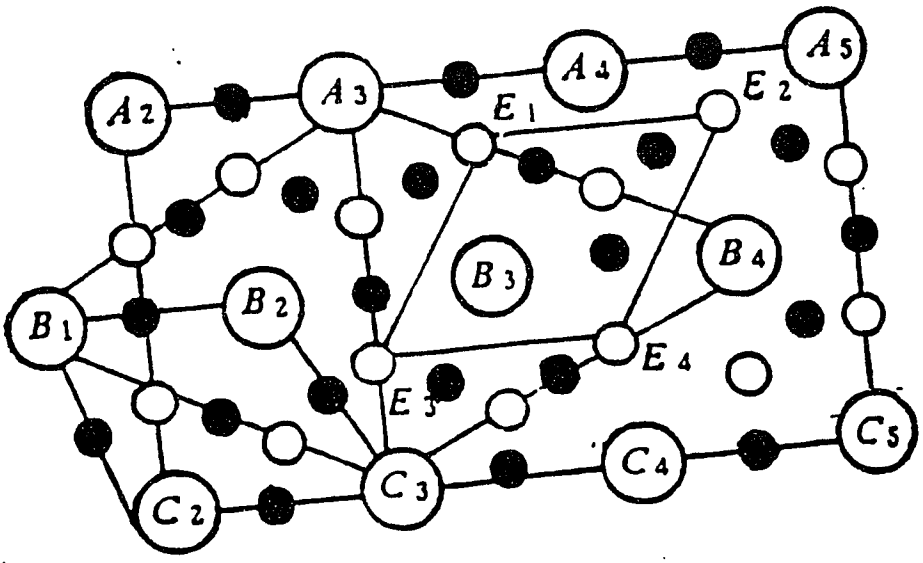

Figure 2.3

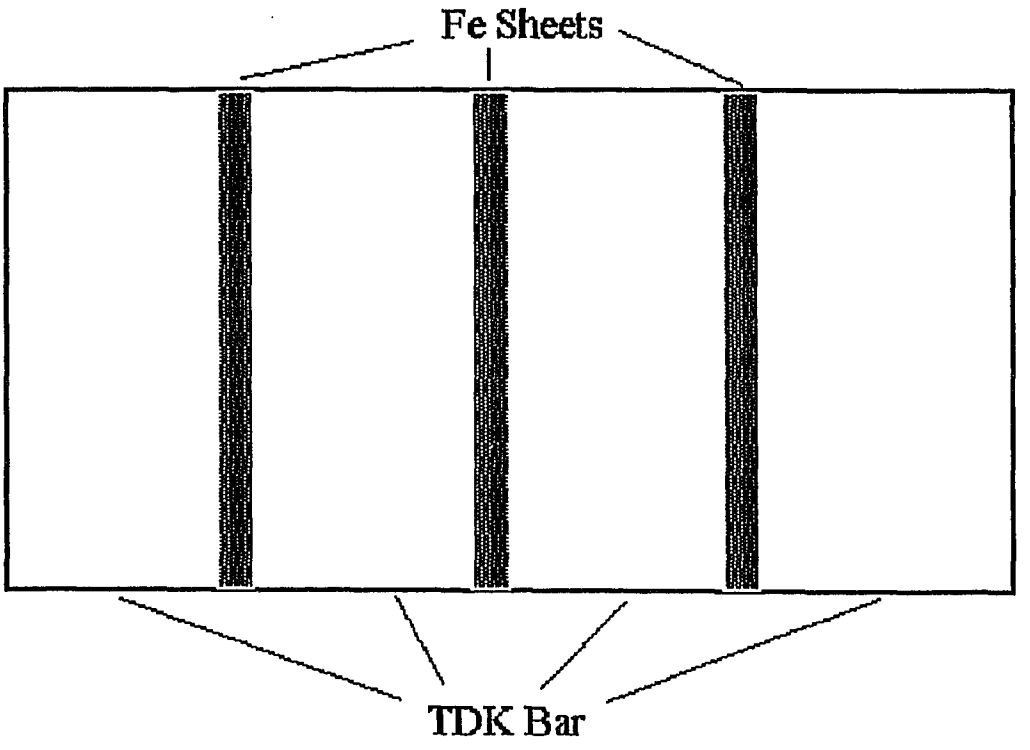

Figure 4.1

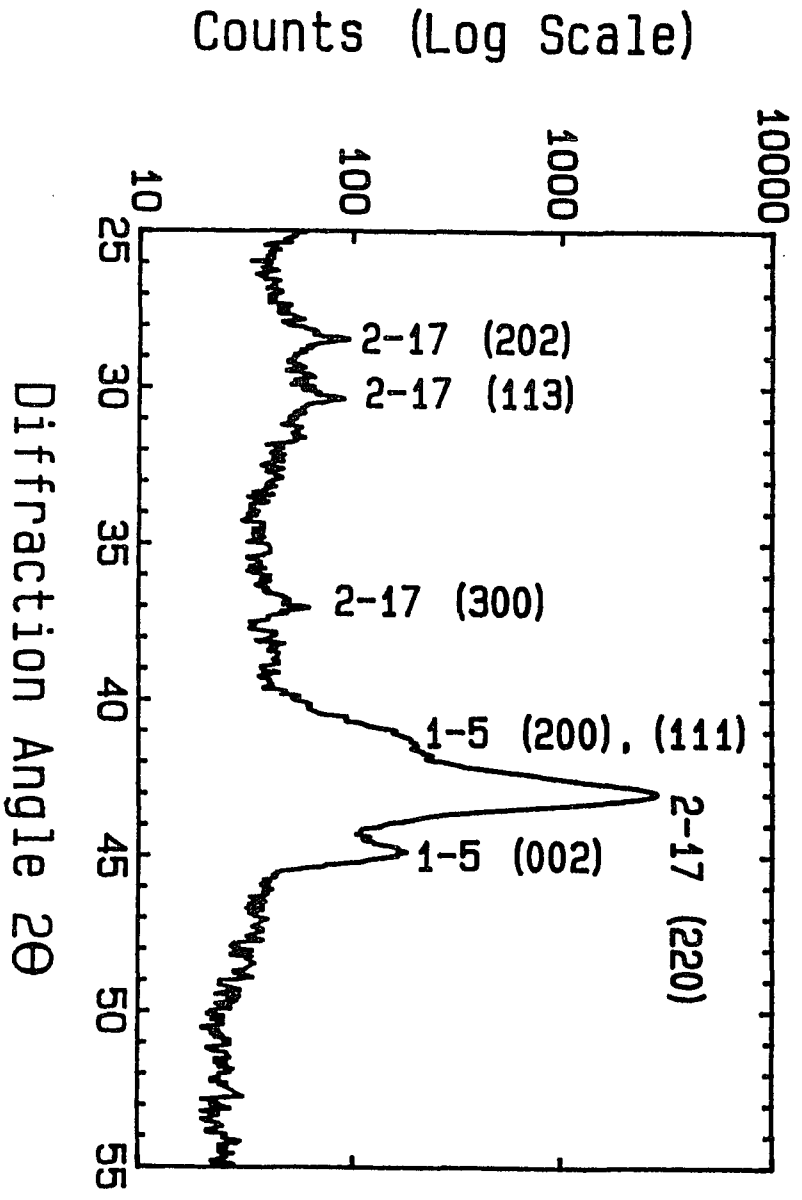
Counts (Log Scale)
10
100
1000
10000
25
30
35
40
45
50
55
Diffraction Angle 2θ
2-17 (202)
2-17 (113)
2-17 (300)
1-5 (200), (111)
2-17 (220)
1-5 (002)

Figure 4.2

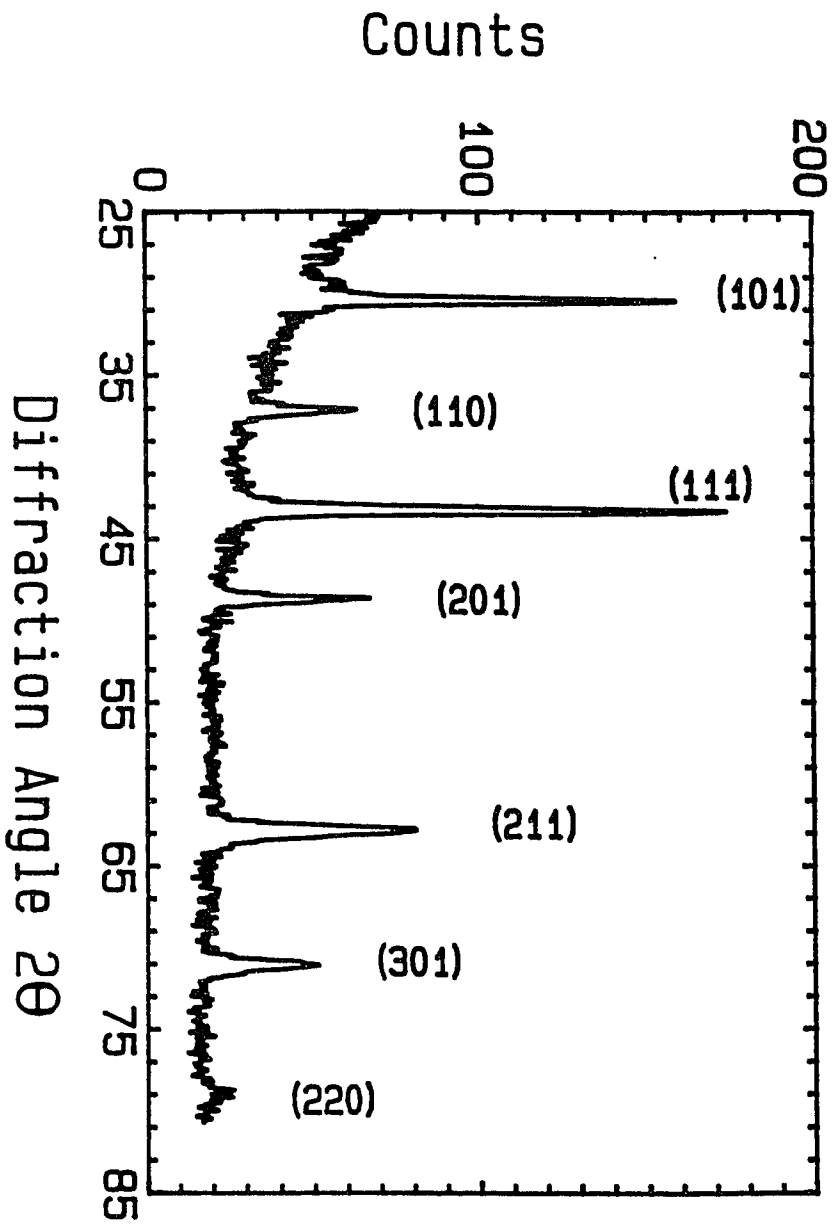
Counts
0
100
200
25
35
45
55
65
75
85
Diffraction Angle 2θ
(101)
(110)
(111)
(201)
(211)
(301)
(220)

Figure 4.3

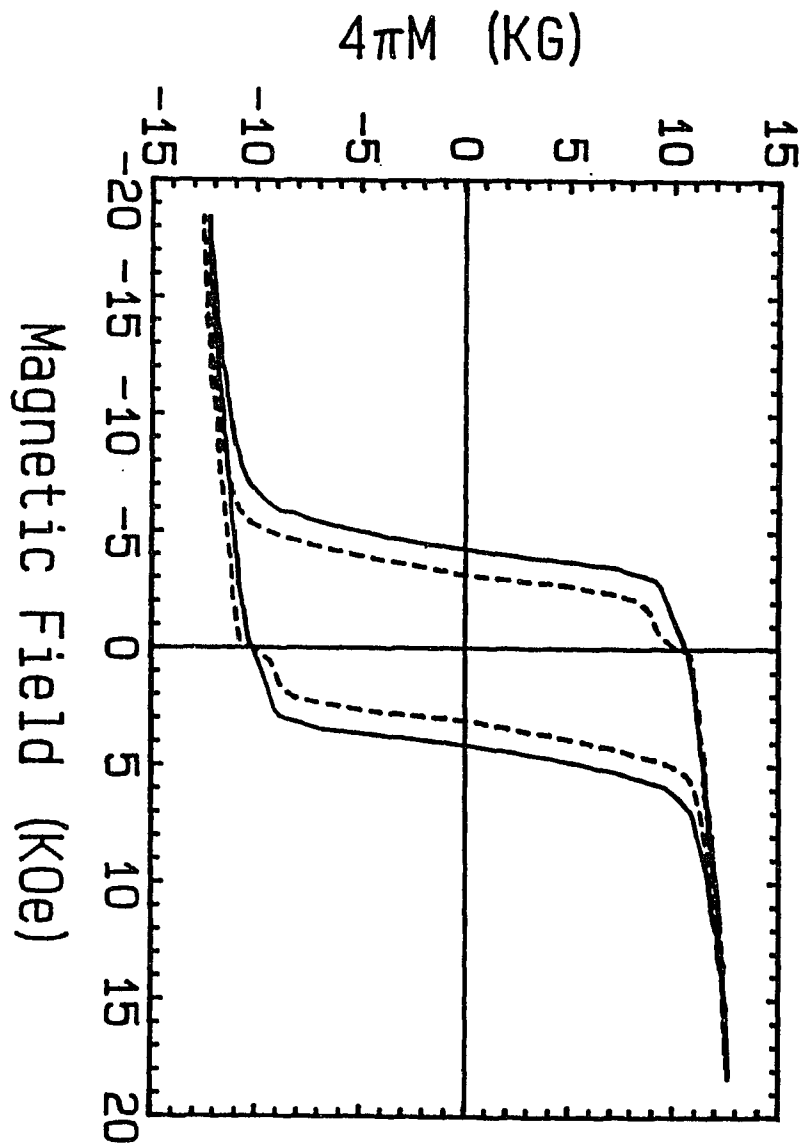

Figure 4.4

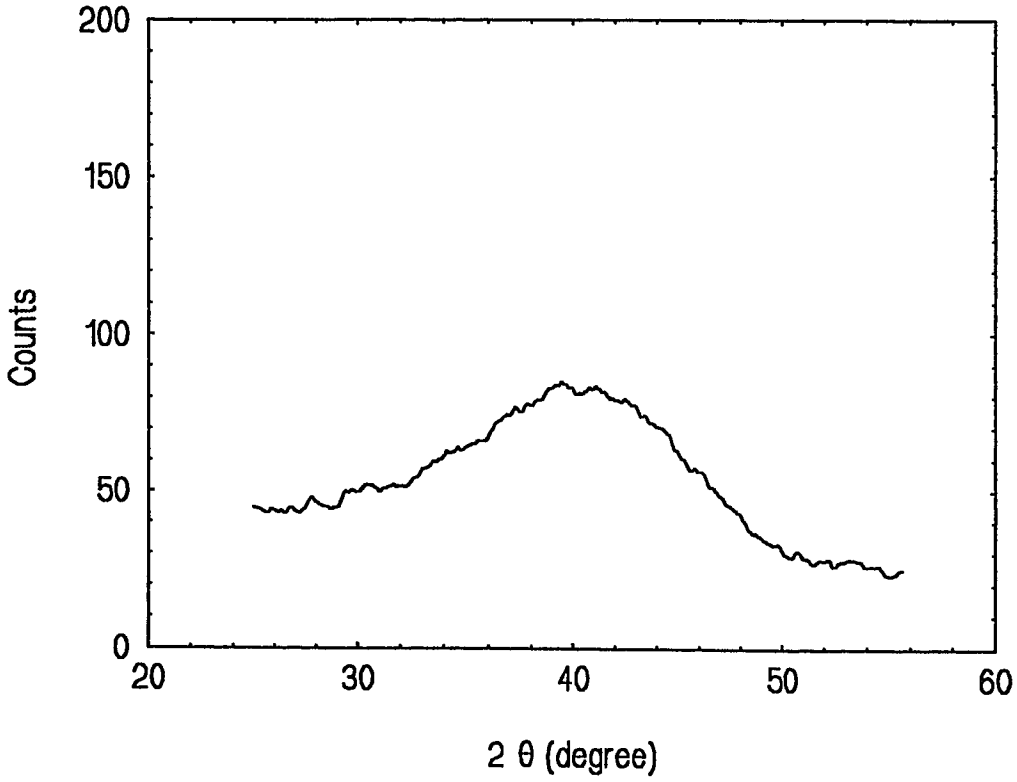

Figure 5.1

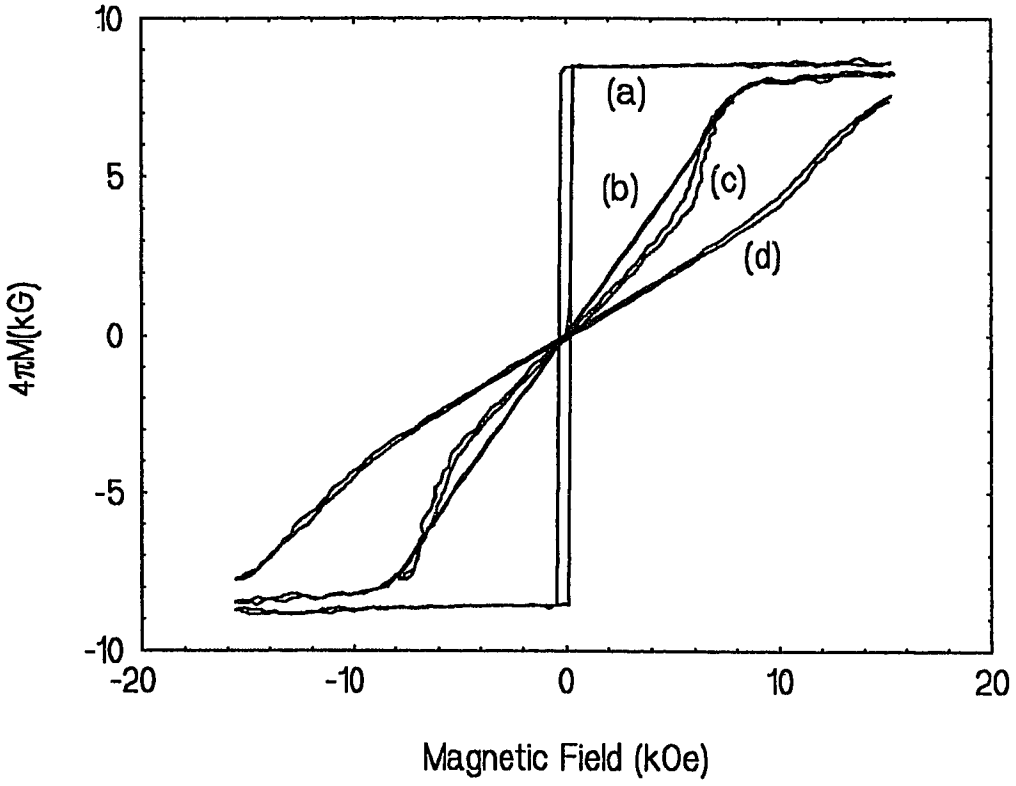

Figure 5.2

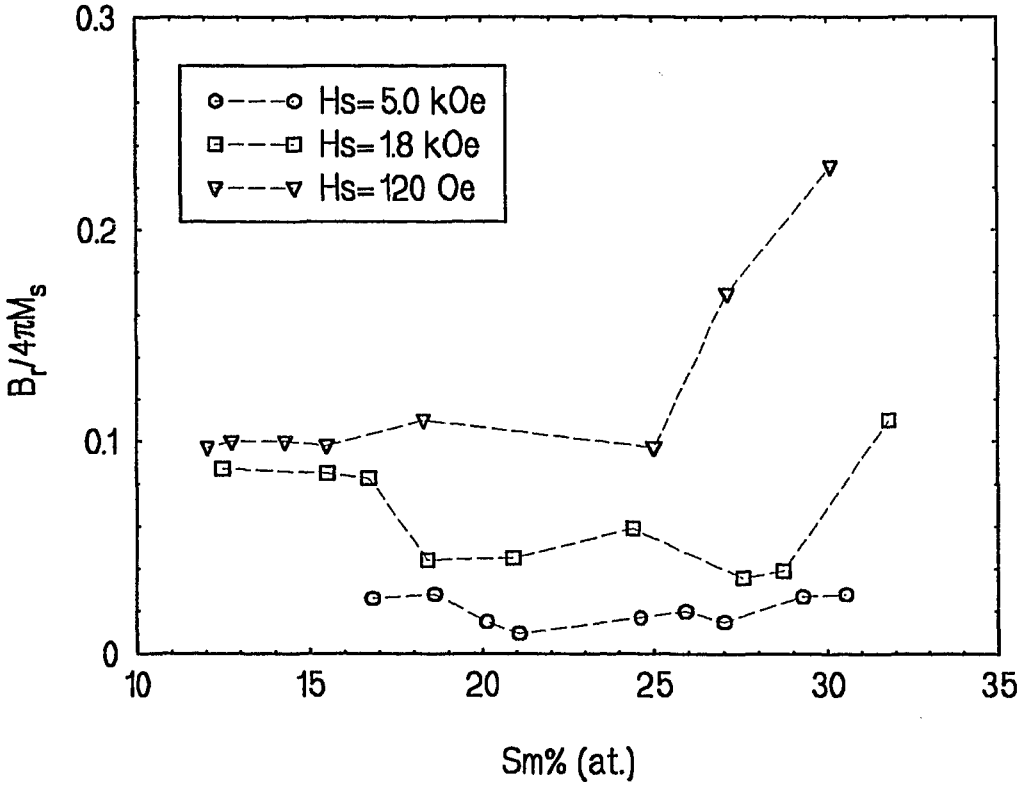
Hs= 5.0 kOe
Hs= 1.8 kOe
Hs= 120 Oe
$B_r/4\pi M_s$
0.3
0.2
0.1
0
10
15
20
25
30
35
Sm% (at.)

Figure 5.3

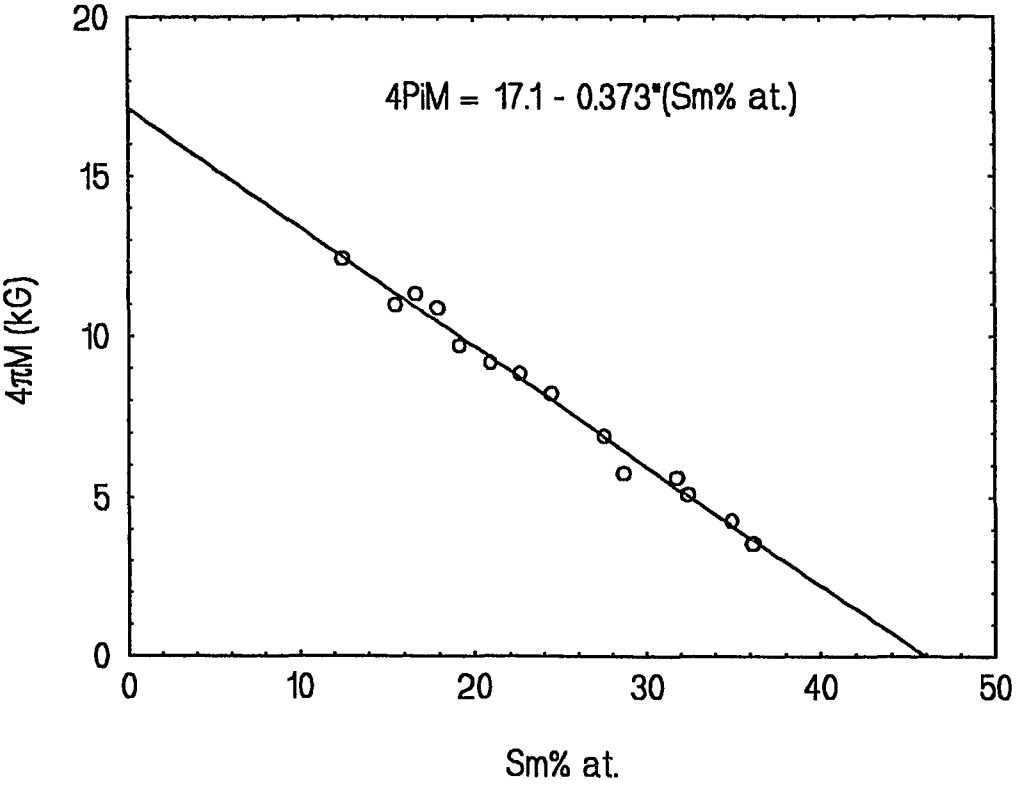

Figure 5.4

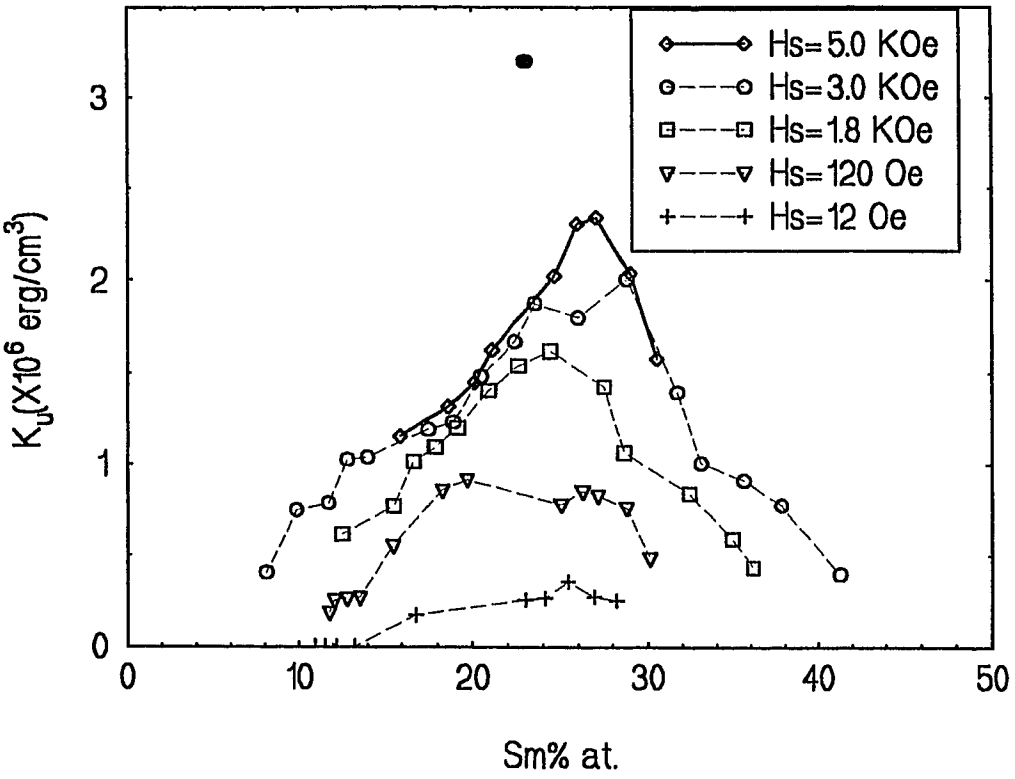
Hs=5.0 KOe
Hs=3.0 KOe
Hs=1.8 KOe
Hs=120 Oe
Hs=12 Oe
K_u(X10^6 erg/cm^3)
Sm% at.
0
1
2
3
0
10
20
30
40
50

Figure 5.5

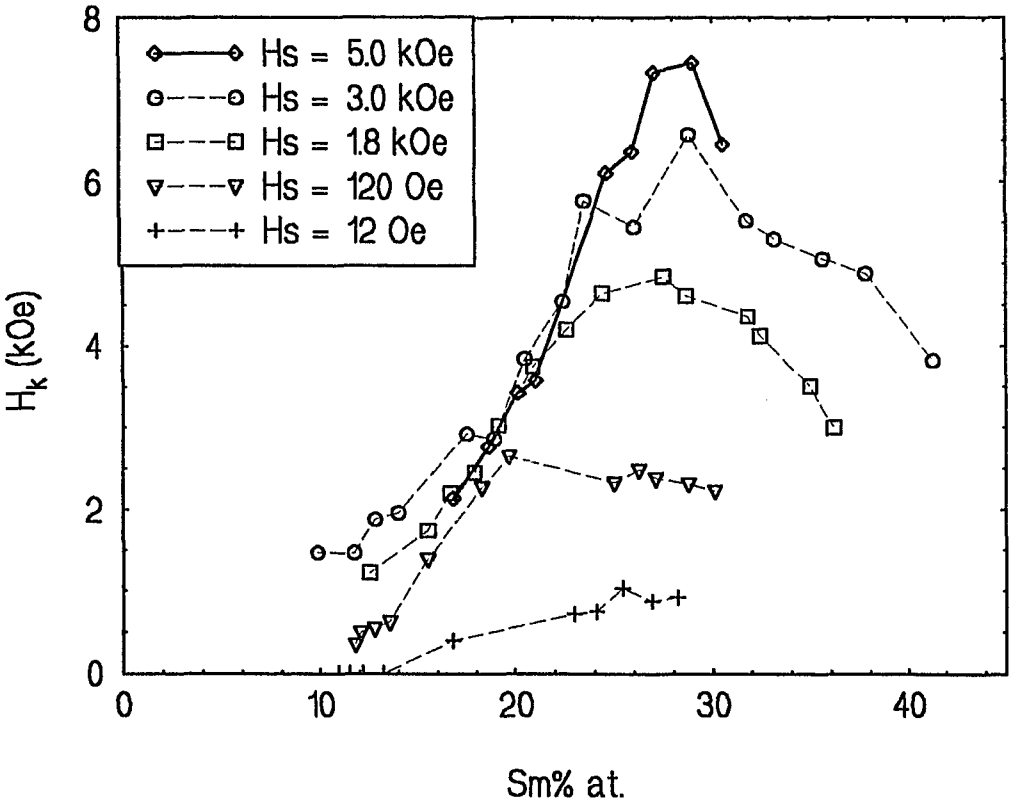
Hs = 5.0 kOe
Hs = 3.0 kOe
Hs = 1.8 kOe
Hs = 120 Oe
Hs = 12 Oe
H_k (kOe)
Sm% at.
0
2
4
6
8
0
10
20
30
40

Figure 5.6

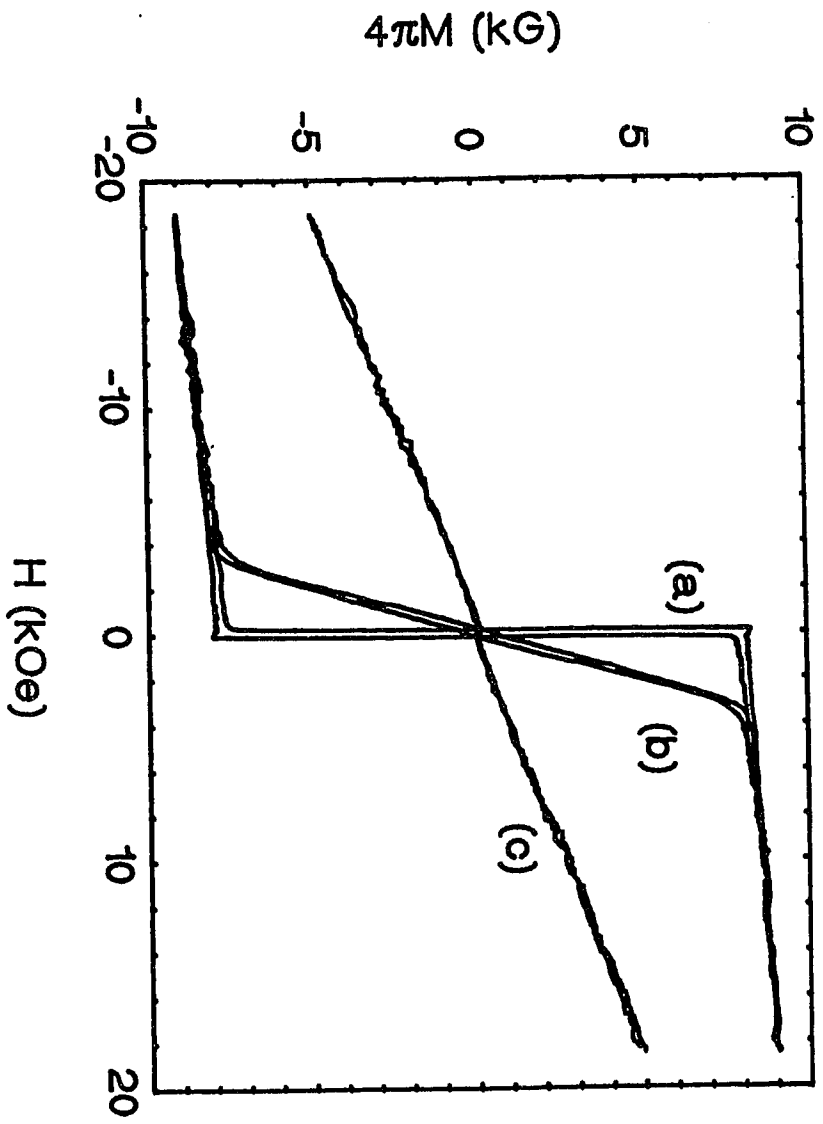

Figure 5.7

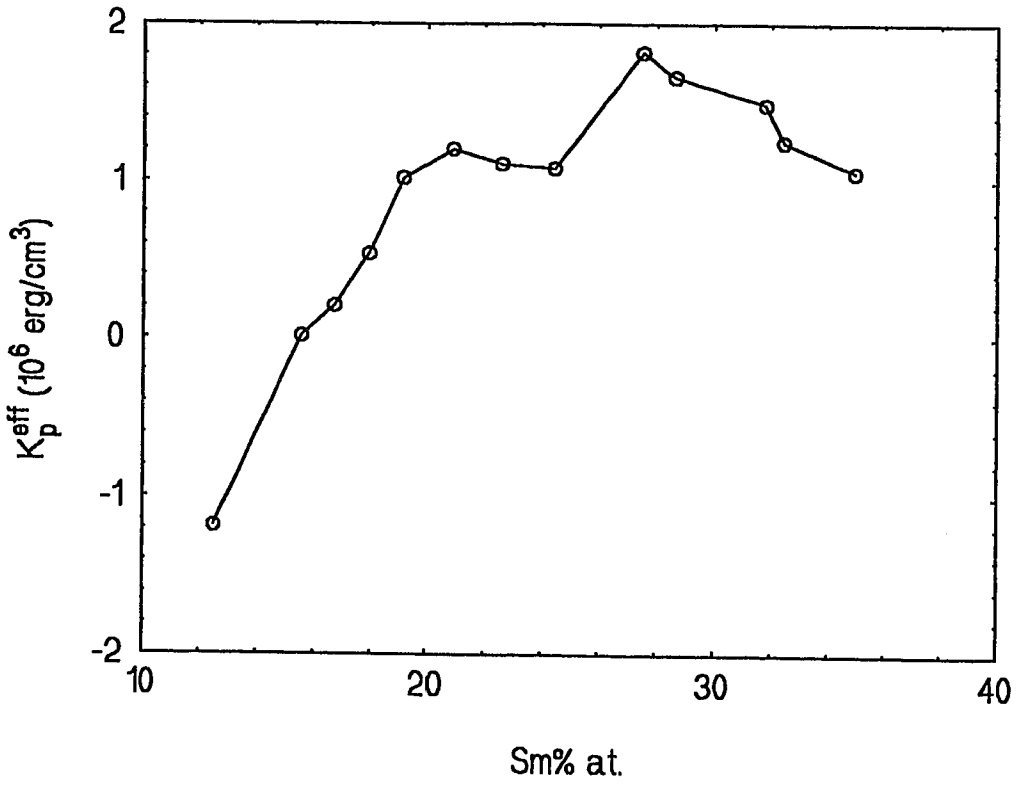

Figure 5.8

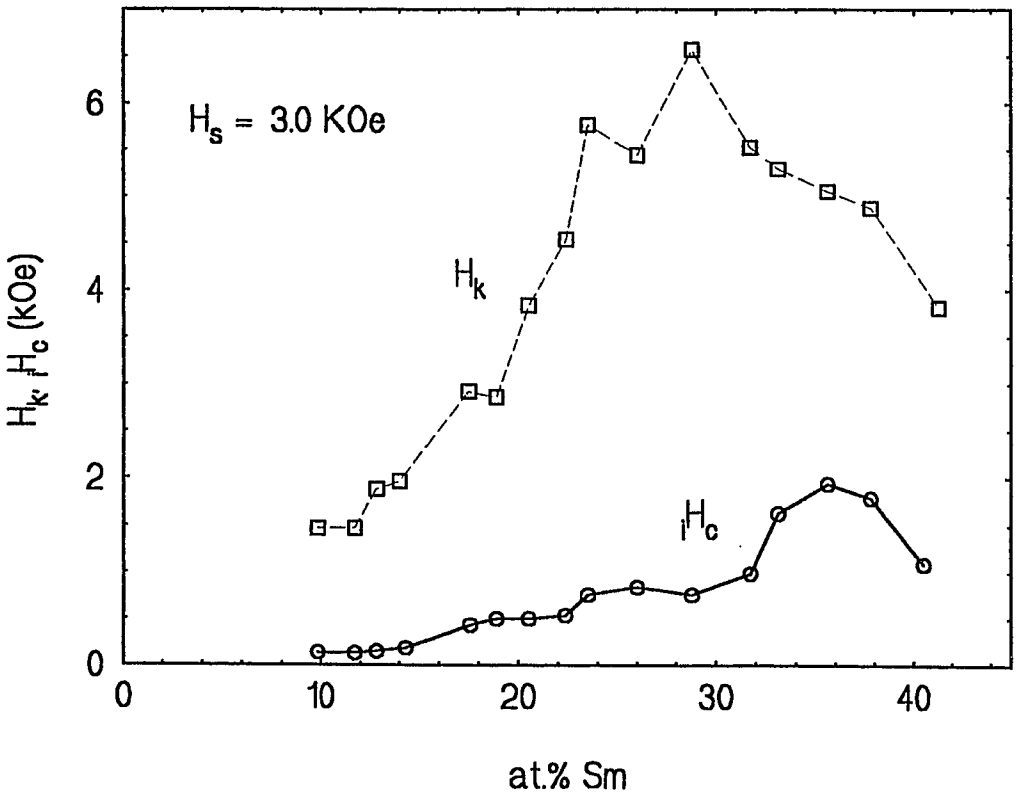

Figure 5.9

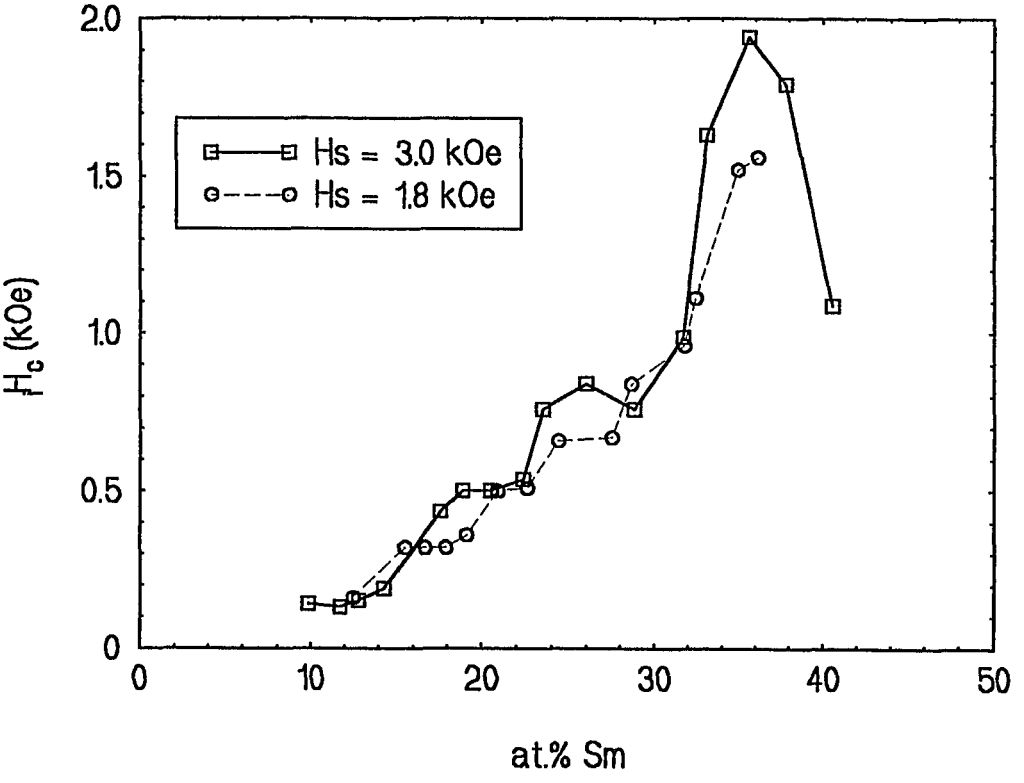

Figure 5.10

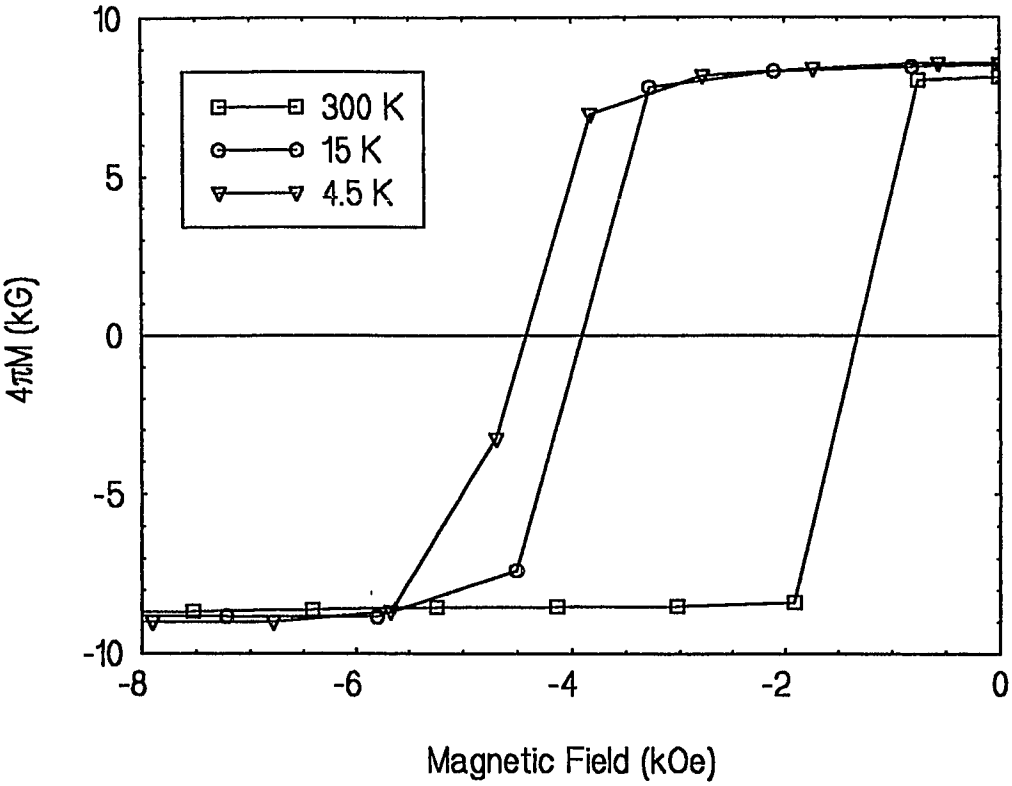

Figure 5.11

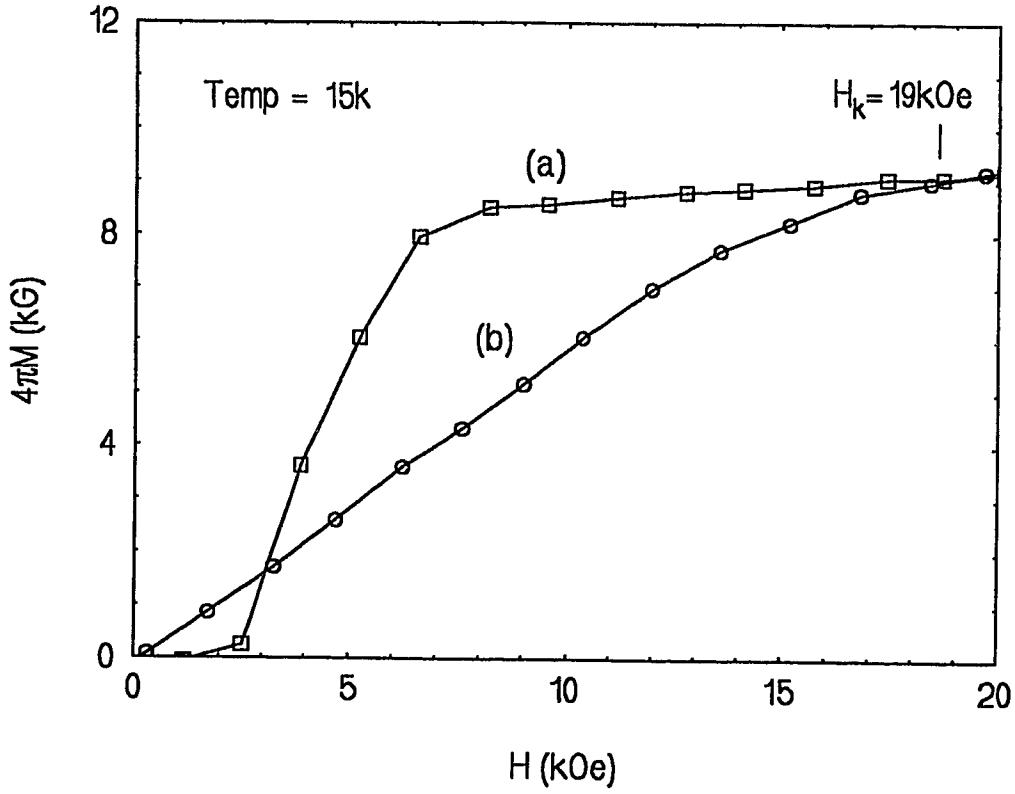

Figure 5.12

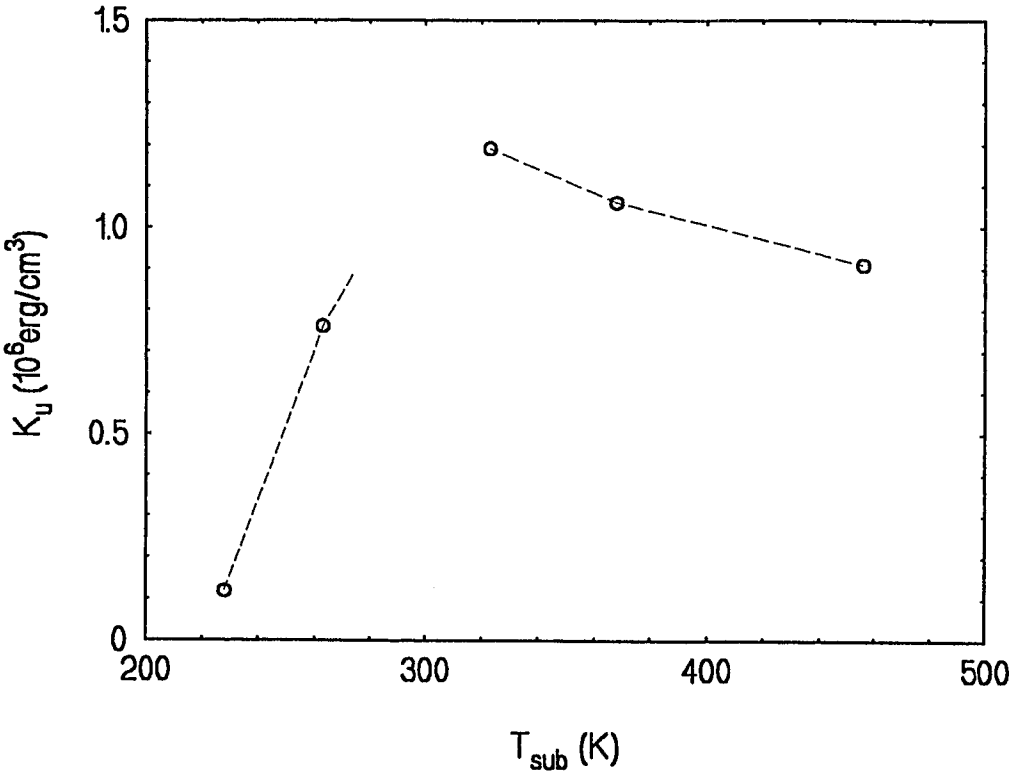

Figure 5.13

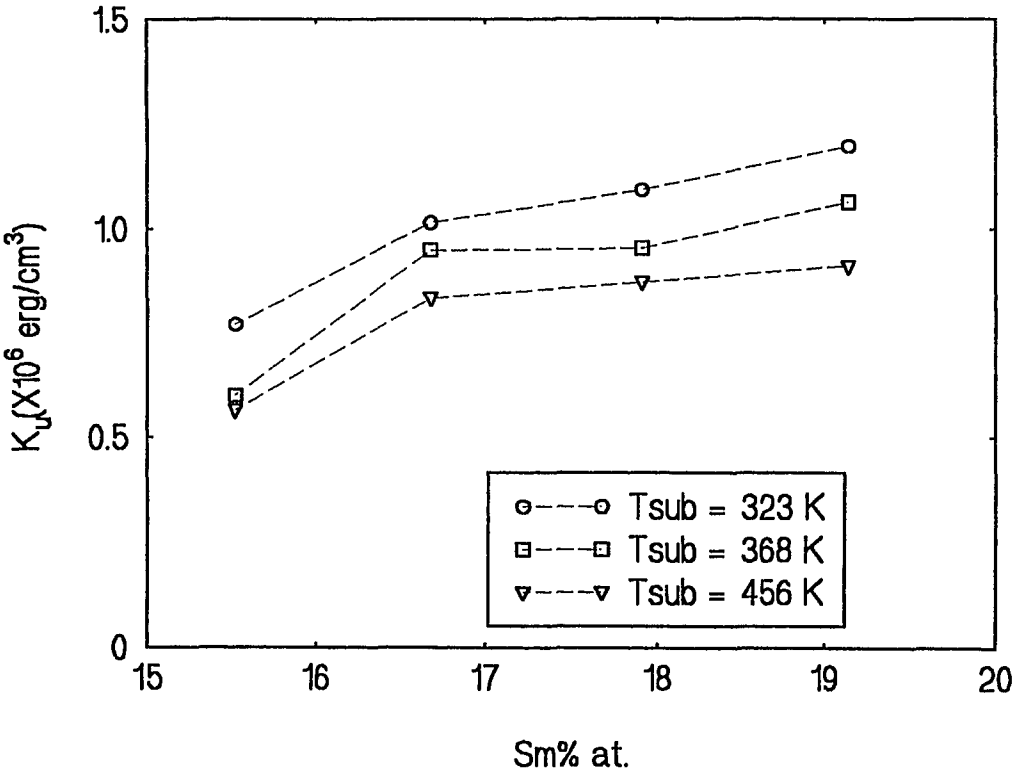
1.5
1.0
0.5
0
15
16
17
18
19
20
K_u (X10^6 erg/cm^3)
Sm% at.
Tsub = 323 K
Tsub = 368 K
Tsub = 456 K

Figure 5.14

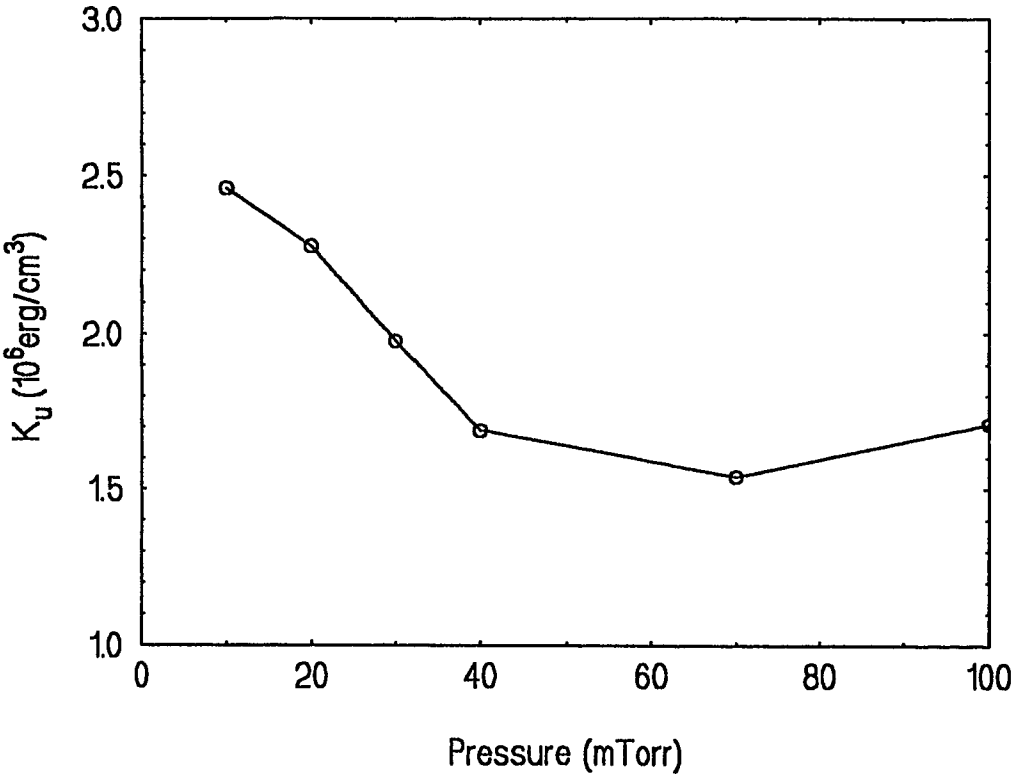

Figure 5.15

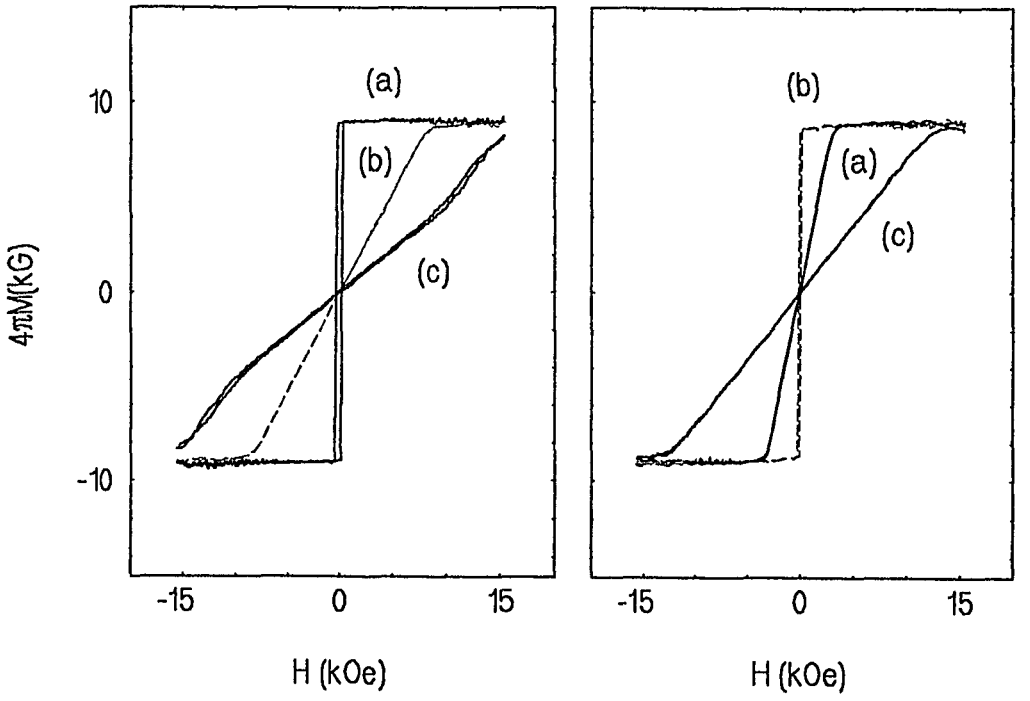

Figure 5.16

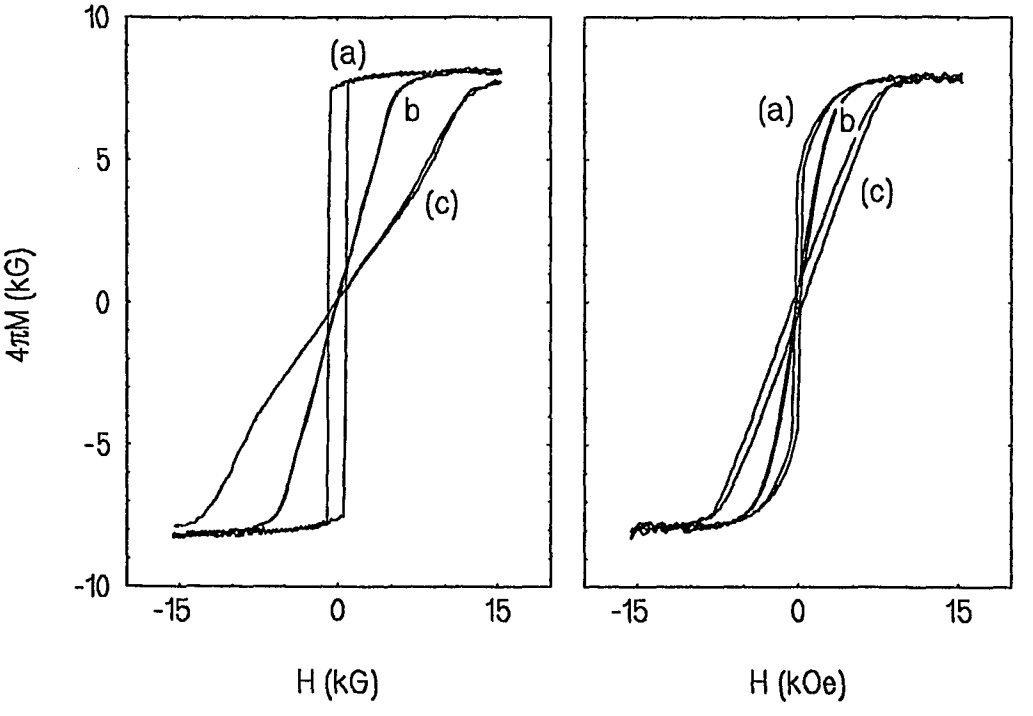

Figure 5.17

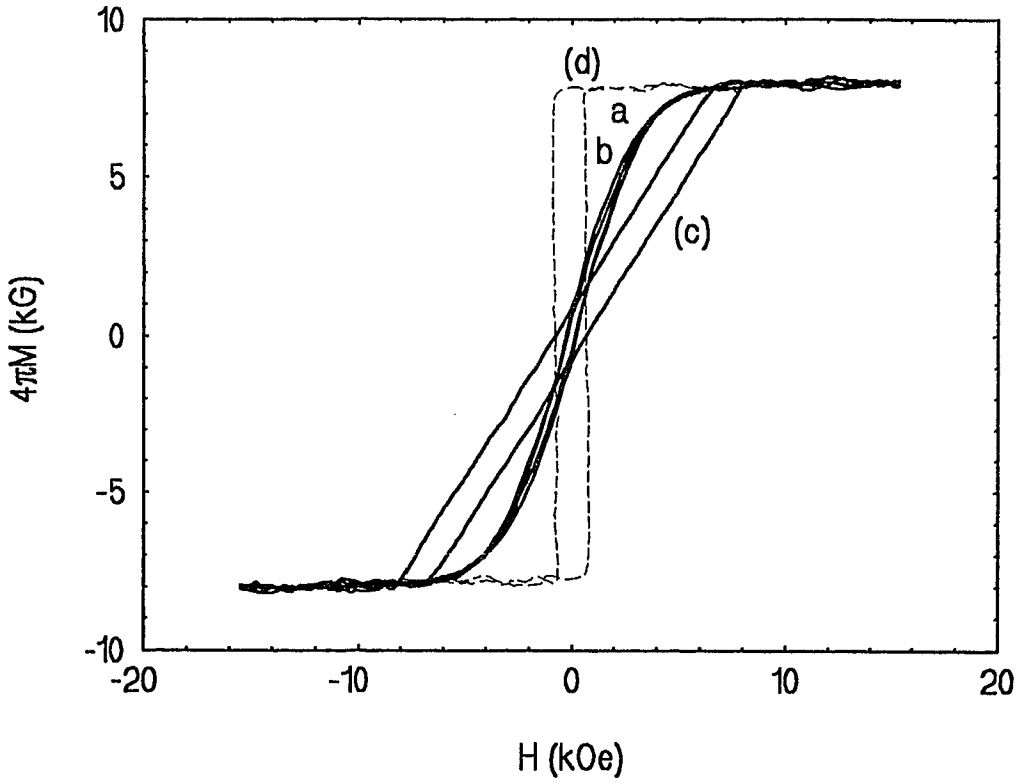

Figure 5.18

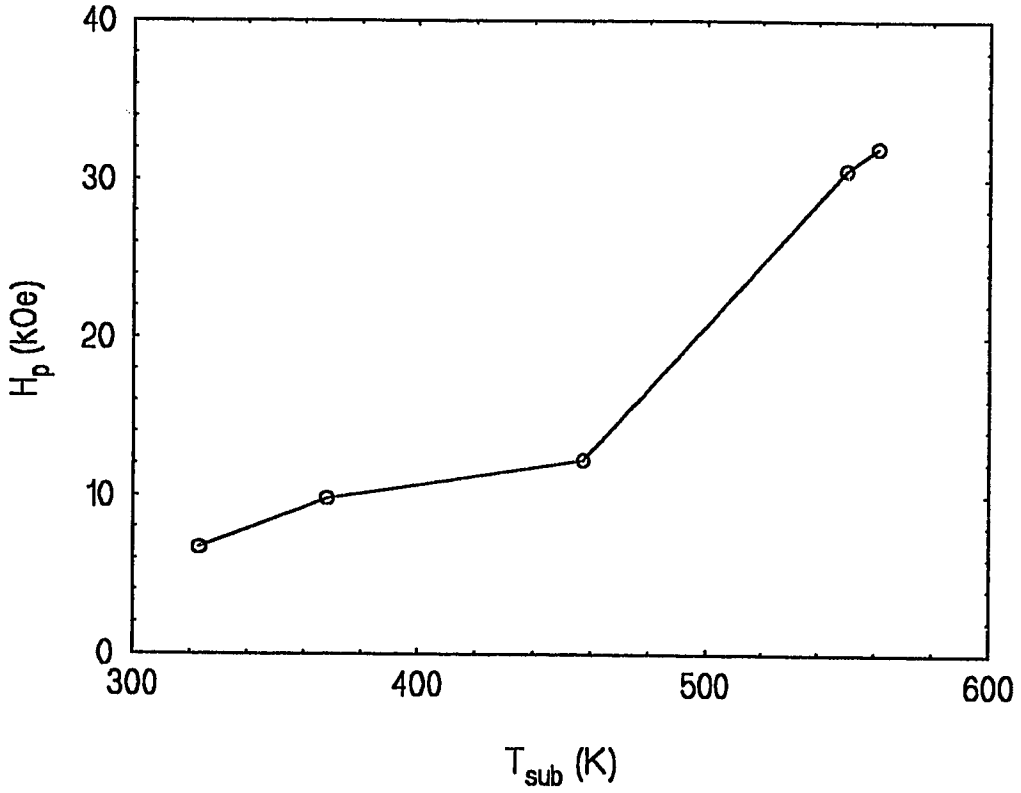

Figure 5.19

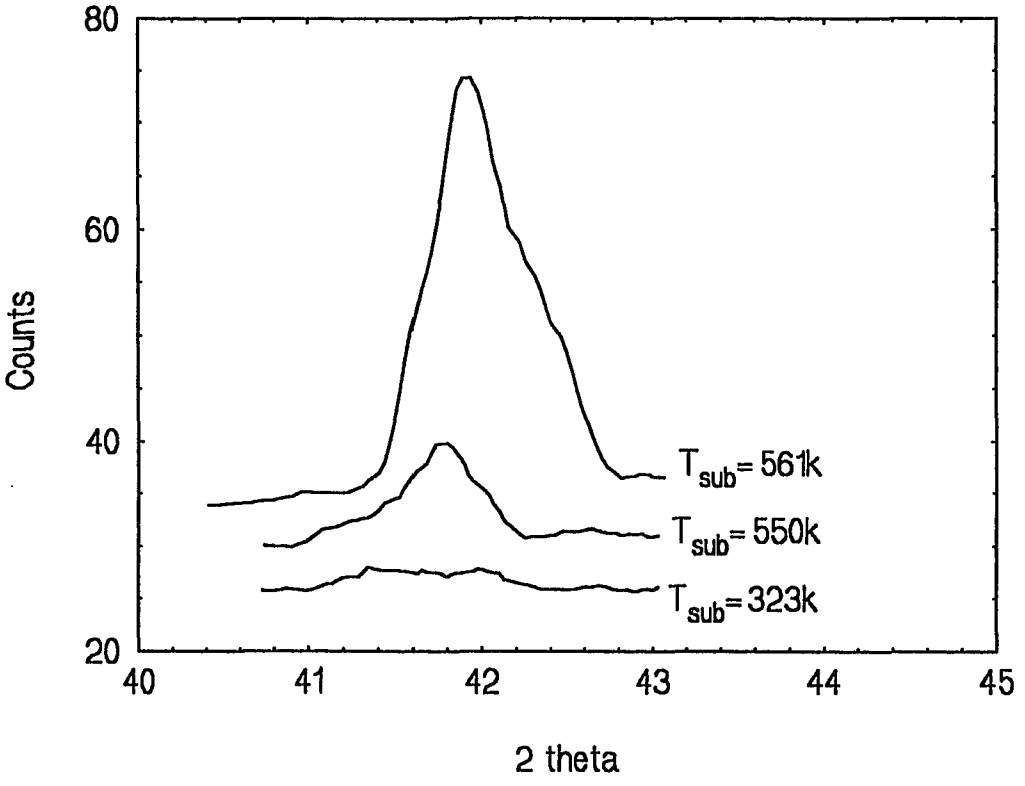
80
60
40
20
Counts
40
41
42
43
44
45
2 theta
T_{sub}= 561k
T_{sub}= 550k
T_{sub}= 323k

Figure 5.20

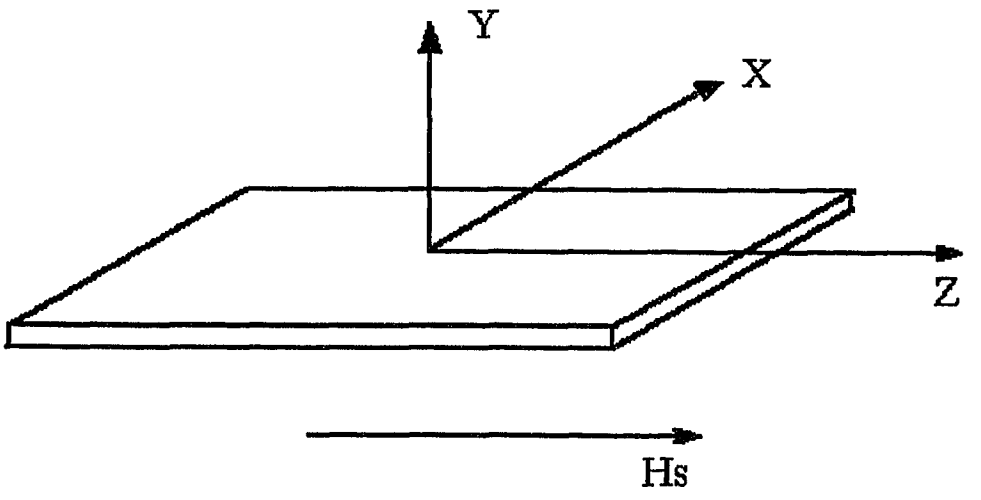

Figure 5.21

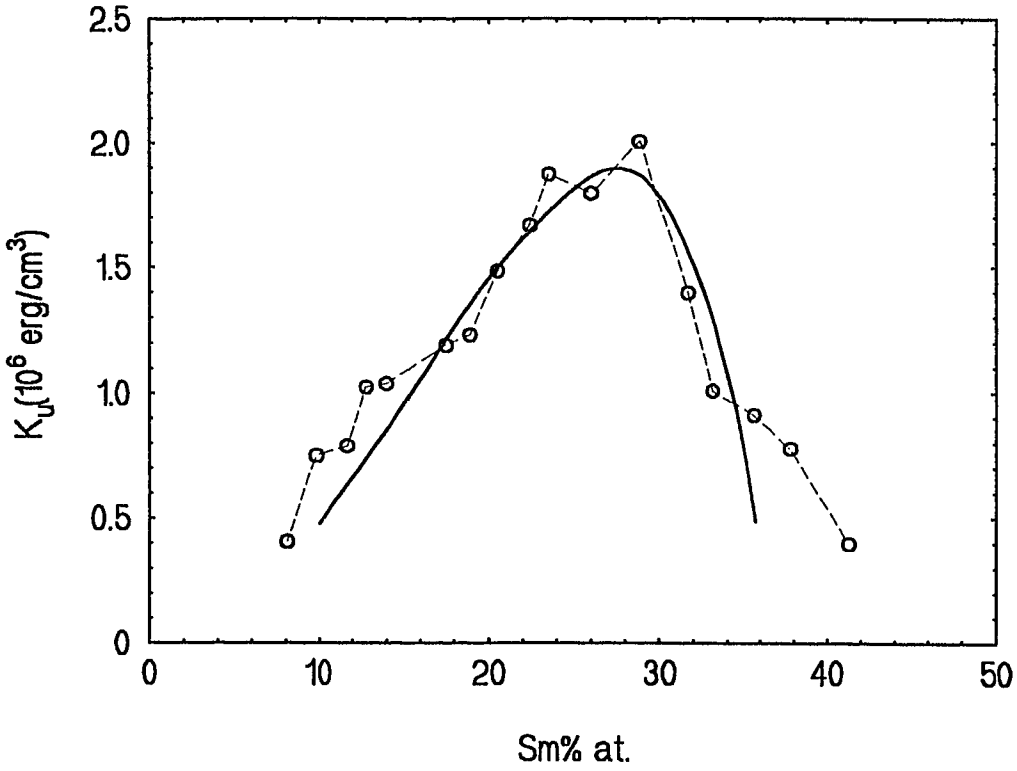

Figure 5.22

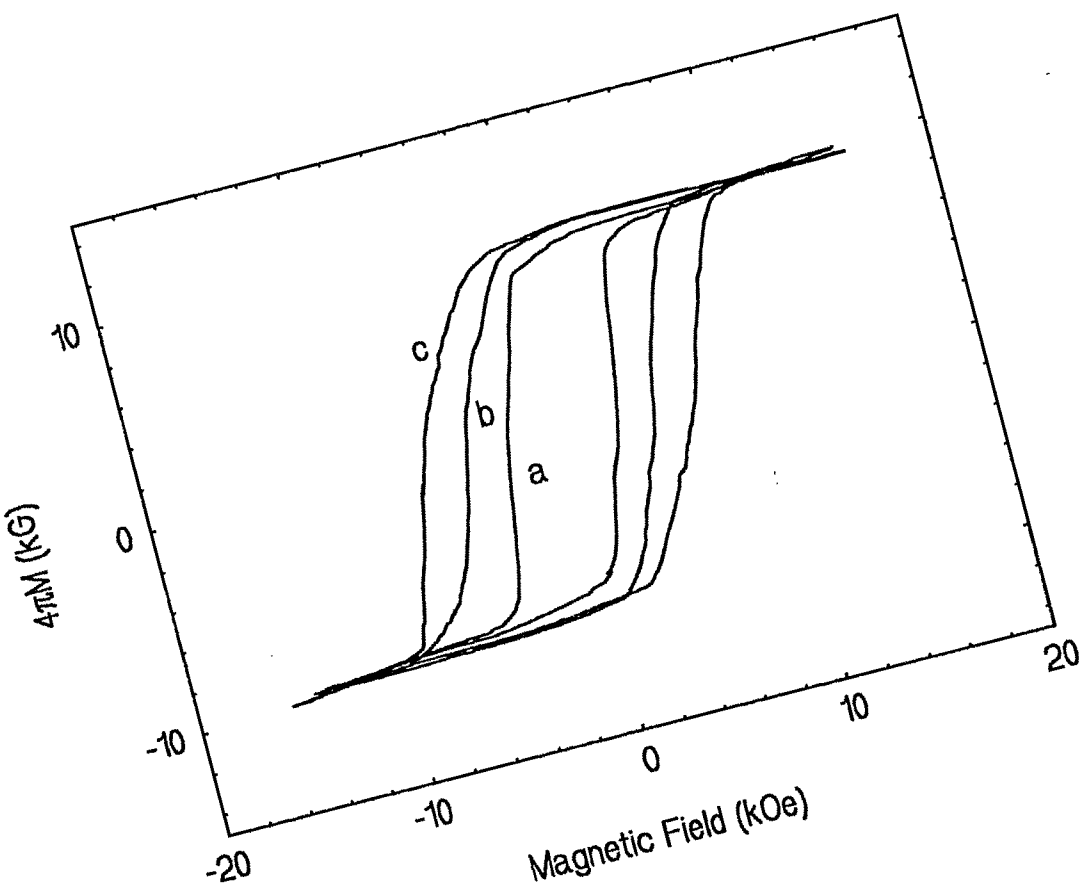

Figure 6.1

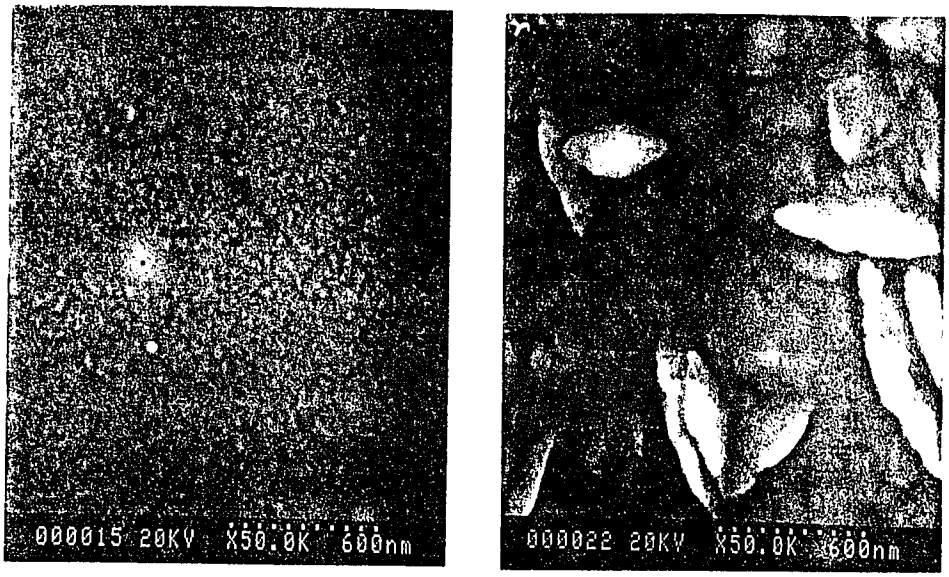

Figure 6.2

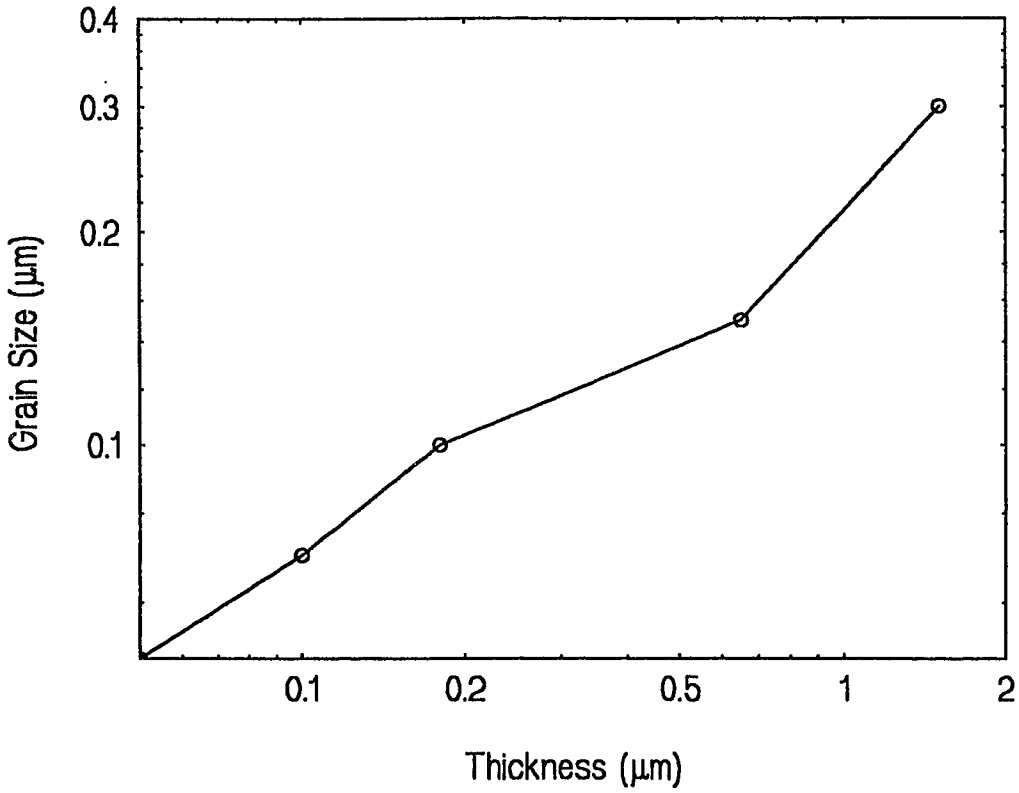

Figure 6.3

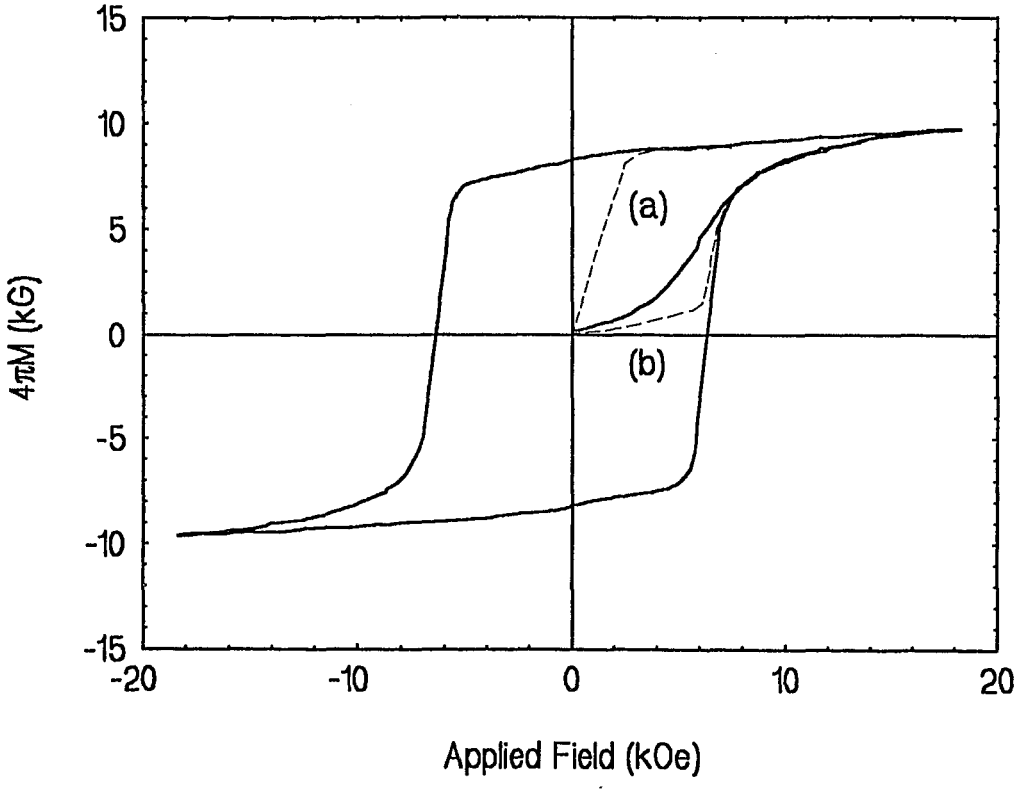

Figure 6.4

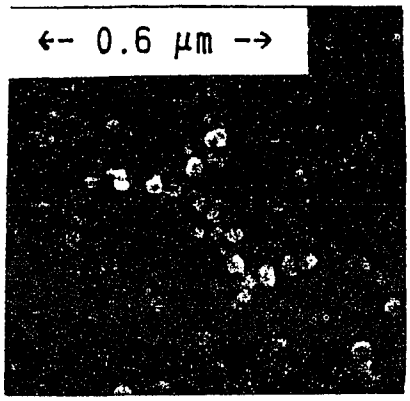

Fig.1. SEM micrograph (x 50000) of a subsequently crystallized film showing grain sizes of the order of 600Å.

Figure 7.1

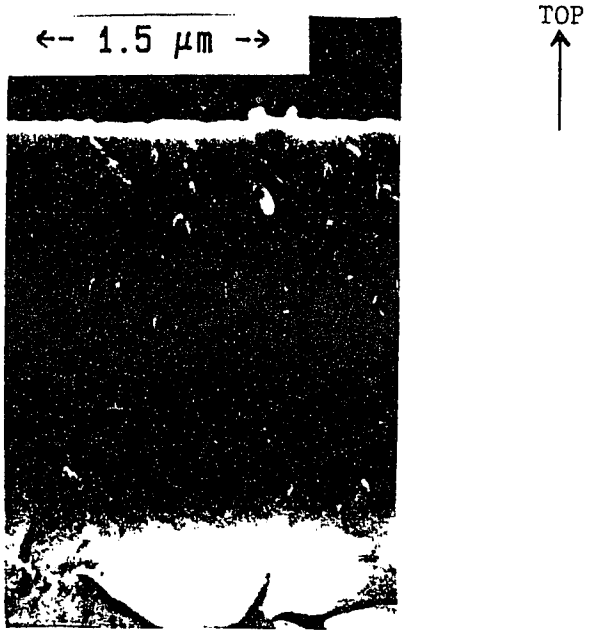

Fig.2. SEM micrograph (x 20000) of the fractured edge of a two layered film.

Figure 7.2

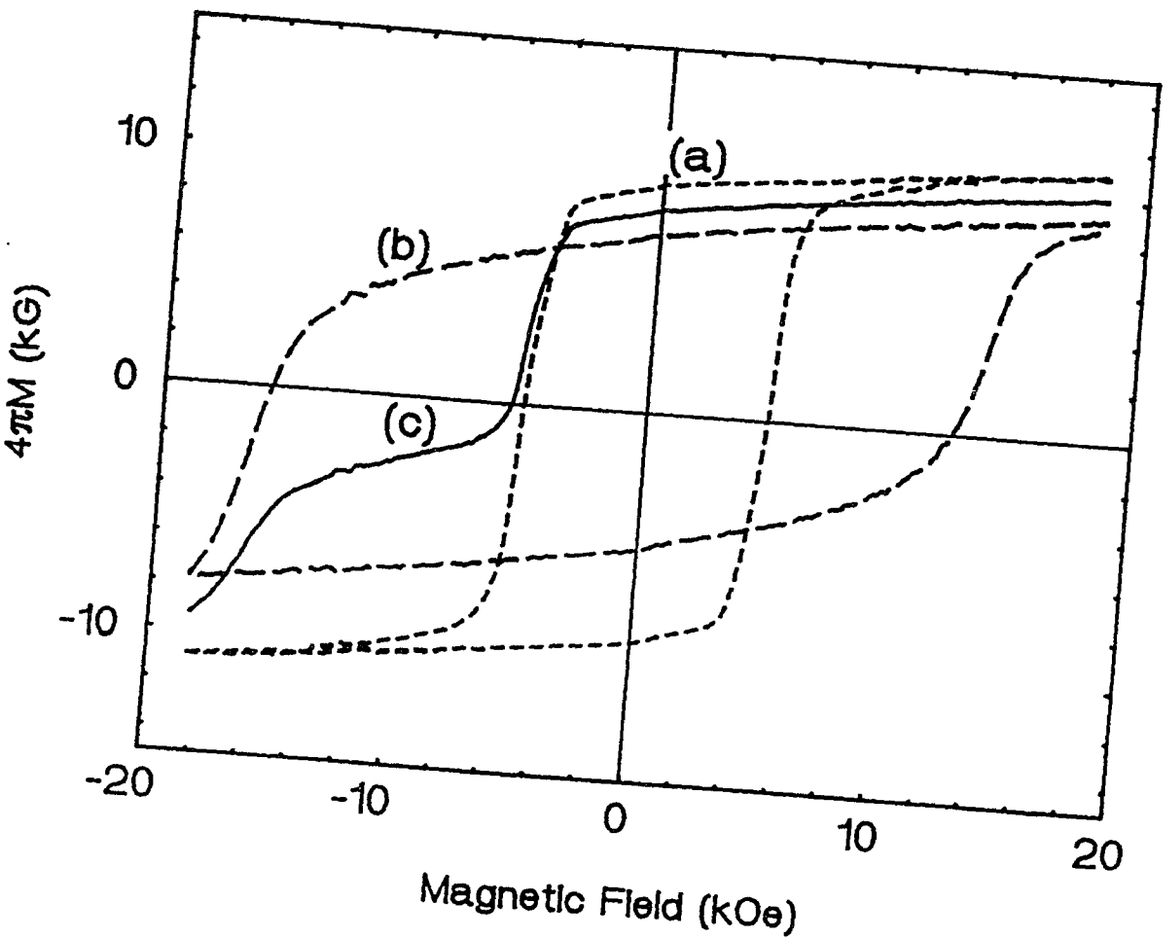

Figure 7.3

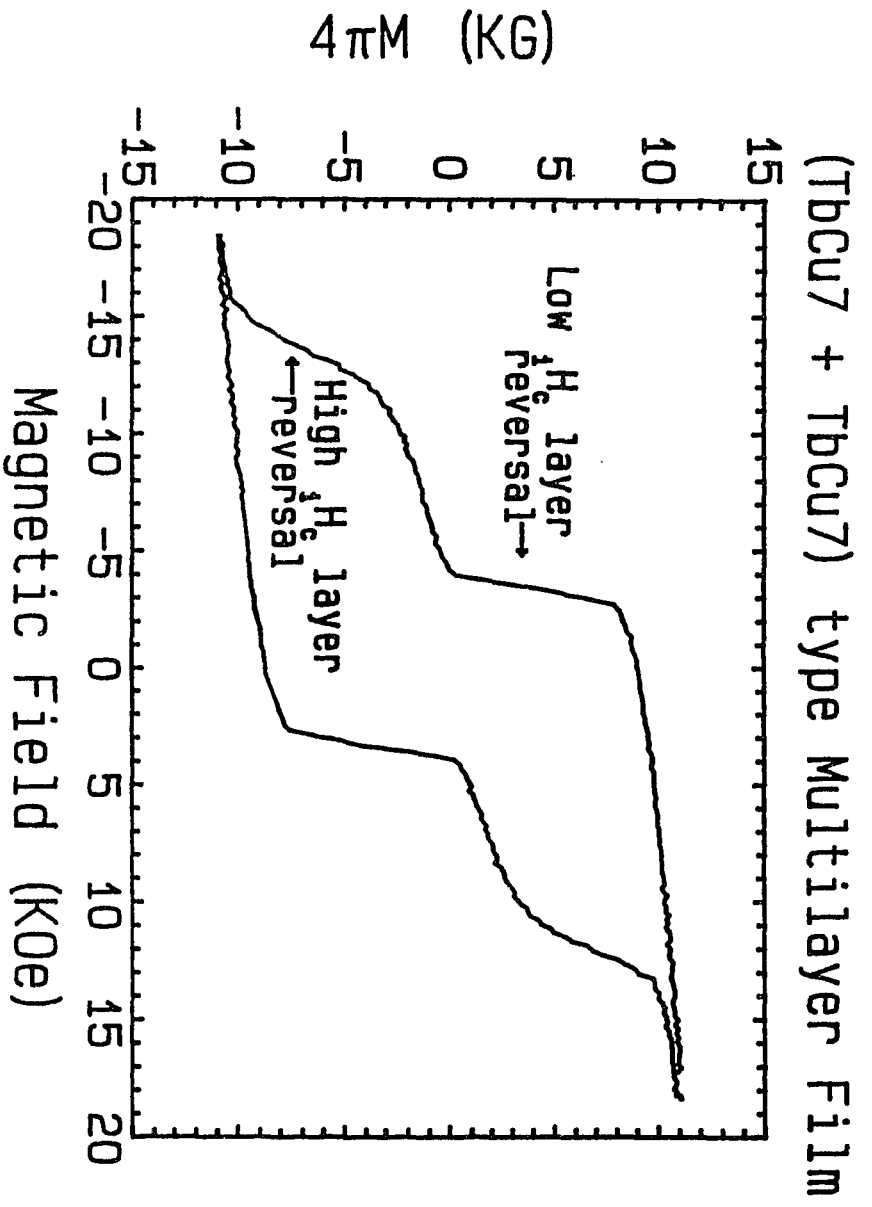
4πM (KG)
15
10
5
0
-5
-10
-15
-20 -15 -10 -5 0 5 10 15 20
Magnetic Field (KOe)
(TbCu7 + TbCu7) type Multilayer Film
Low H_c layer Reversal
High H_c layer Reversal

Figure 7.4

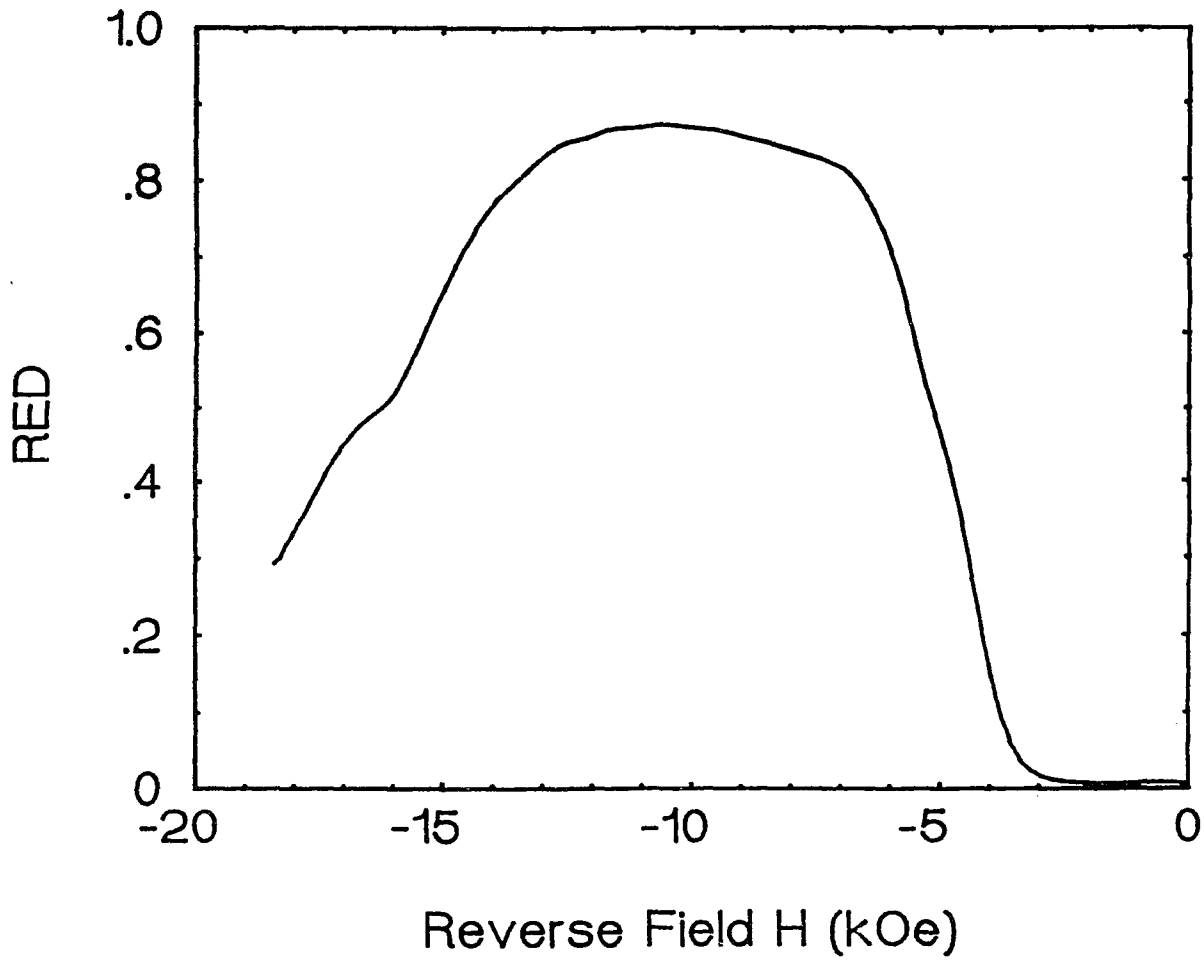

Figure 7.5

REFERENCES:

1. F. J. Cadieu, Thin film physics (Academic, San Diego, 1992), Vol.16, p. 169.

2. K. E. Johnson, J. Appl. Phys. 69, 4932(1991)

3. K. Kumar, J. Appl. Phys. 63, R13(1988)

4. J. F. Herbst, Rev. Mod. Phys. 63, 819(1991)

5. F.J. Cadieu, H. Hegde, and K. Chen, J. Appl. Phys. 67, 4969(1990)

6. F.J. Cadieu, H. Hegde, and K. Chen. IEEE Trans. on Magnetics, MAG-25, 3788(1989)

7. F.J. Cadieu, H. Hegde, and K. Chen, Thin Solid Films 193/194, 857(1990)

8. H. Hegde, R. Rani, A. Navarathna, K. Chen and F. J. Cadieu, J. Appl. Phys. 70, 6345(1991)

9. F. J. Cadieu, H. Hegde, A. Navarathna, R. Rani, and K. Chen, Appl. Phys. Lett. 59, 875(1991)

10. H. Hegde, K. Chen and F. J. Cadieu, J. Appl. Phys. 69, 5850(1991)

11. T.D. Cheung, L. Wickramasekara, and F.J. Cadieu, J. Appl. Phys. 57, 3598(1985)

12. U. Kullmann, B. Koester, and C. Dorsch, IEEE Trans. Magn., MAG-20, 420(1984)

13. H.A.M. van den Berg, K. Schuster, G. Rupp, A. Schone-Warnefeld, and W. Marko, IEEE Trans. Magn., MAG-25, 3344(1989)

14. G. Suran, K. Ounadjela, and F. Machizaud, Phys. Rev. Lett. 57, 3109(1986).

15. K. Ounadjela, G. Suran, and F. Machizaud, Phys. Rev. B 40, 578(1989)

16. K. Chen, H. Hegde, and F. J. Cadieu, Appl. Phys. Lett. 61, 1861(1992)

17. K. Chen, H. Hegde, S.U. Jen, and F. J. Cadieu, 37th Conference on Magnetism and Magnetic Materials, Paper CP-22, 1992, J. Appl. Phys., (to be published)

18. K. Chen, H. Hegde, and F.J. Cadieu, J. Appl. Phys. 69, 6064(1991)

19. B.D. Cullity, Introduction to Magnetic Materials (Addison Wesley, New York, 1972)

20. S. Chikazumi, ch. 3, Physics of Magnetism, John Wiley and Son, New York, 1964.

21. J. H. Wernick, S. Geller, Acta Cryst. 12, 662(1959)

22. Y. Khan, Acta Cryst. B29, 2502(1973)

23. K.H. Buschow and A.S.Van der Goot, J. Less Common Metals, 37, 174(1974)

24. W.E.Wallace, Prog. Rare Earth Sci. and Tech., vol. 3, 1(1968)

25. I.A. Campbell, J. Phys. F 2, L47(1972)

26. K. J. Strnat, G. Hoffer, W. Ostertag, and J.C. Olson, J. Appl. Phys. 37, 1252(1966)

27. J.J. Becker, J. Appl. Phys. 41, 1055(1970)

28. K.H.J. Buschow, Phys. Status Solidi, A7, 199(1971)

29. K.H.J. Buschow, Rep. Prog. Phys. 40, 1179(1977).

30. A.S. Ermolenko, IEEE Trans. Magn. MAG-12, 992(1976)

31. J.E. Greedan and V.U.S. Rao, J. Solid State Chem. 6, 387(1973)

32. S.G. Sankar, V.U.S. Rao, E. Segal, W.E. Wallace, W.G.D. Frederick, and H.J. Garrett, Phys. Rev. B 11, 435(1975).

33. S. Chikazumi, p.147, Physics of Magnetism, John Wiley and Son, New York, 1964.

34. F. Seitz, The Modern Theory of Solids (McGraw Hill, New York, 1940), p. 427.

35. B. Chapman, Glow Discharge Processes, (Wiley Interscience, 1980).

36. Thin Film Processes, ed. by J.L.Vossen and Werner Kern (Academic Press, 1978)

37. O.C. Wells, Acanning Electron Microscopy, (McGraw-Hill, New York, 1974).

38. H. Hegde, Ph.D thesis, City University of New York, 1990.

39. J. Deportes, D. Givord, R. Lemaire, H. Nagai, and Y. T. Yang, J. Less-common Metals 44, 273(1976)

40. S. Liu and A. E. Ray, IEEE Trans. Magn. MAG-25, 3785(1989).

41. P. Chaudhari, J.J. Cuomo, and R.J. Gambino, IBM J. Res. Dev. 11, 66(1973).

42. R.J. Gambino, P.Chaudhari, and J.J. Cuomo, in Magnetism and Magnetic Materials, Proceedings of the 19th annual Conference, Boston, 1973, AIP conf. Proc. No. 18 (AIP, New York, 1973), p. 578.

43. H. Kobayashi, T. Ono, A. Tsushima, and T. Suzuki, Appl. Phys. Lett. 43, 389(1983).

44. R.J. Gambino, J.Ziegler, and J.J. Cuomo, Appl. Phys. Lett. 24, 99(1974).

45. Y. Suzuki, S. Takayama, F. Kirino, and N. Ohta, IEEE Trans. Magn. MAG-23, 2275(1987).

46. Y. Suzuki, J. Haimovich, and T. Egami, Phys. Rev. B 35, 2162(1987).

47. X. Yan, T. Egami, and E.E. Marinero, J. Appl. Phys. 69, 5448(1991).

48. F. Hellman, and E.M. Gyorgy, Phys. Rev. Lett. 68, 1391(1992).

49. M. Miura, H. Katahashi, K. Muramori, and M. Kajiyama, IEEE Trans. Magn. 24, 2215(1988).

50. H. Fujimori, H. Morita, Y. Obi, and S. Ohta, in Amorphous Magnetism II, edited by R.A. Levy and R. Hasegawa, (Plenum Press, New York and London 1977).

51. G. Suran, J. Sztern, and B. Barbara, Appl. Phys. Lett. **58**, 1338(1991).

52. Xingbo Yang, and T. Miyazaki, J. Appl. Phys. **64**, 5489(1988).

53. F.E. Luborsky, J. Appl. Phys. 57, 3592(1985).

54. K-Y. Ho, J. Appl. Phys. **53**, 7828(1982).

55. F. E. Luborsky, and J. L. Walter, IEEE Trans. on Magnetics, **MAG 13**, 953 (1977).

56. L. Neel, in Selected Works of Louis Neel, edited by Nicholas Kurti, (Gordon and Breach, New York, 1988), p. 387.

57. John C. Slonczewski, p. 205, in Magnetism I, edited by G.T. Rado and H. Suhl, (Academic Press, New York, 1963).

58. S. Chikazumi, p. 359, Physics of Magnetism, John Wiley and Son, New York, 1964.

59. T. Mizoguchi, and G. S. Cargill III, J. Appl. Phys. 50, 3570(1979).

60. C. Tsang, J. Appl. Phys. **55**, 2226 (1984).

61. H. Hegde, S.U. Jen, K. Chen and F. J. Cadieu, 37th Conference on Magnetism and Magnetic Materials, Paper CP-23, 1992, J. Appl. Phys., (to be published).

62. F. J. Cadieu, J. Appl. Phys. 61, 4105(1987).

63. F. J. Cadieu, J. Vac. Sci. Technol. A 6, 1668(1988).

64. F. J. Cadieu, T. D. Cheung, L. Wickramasekara, N. Kamprath, H. Hegde, and N. C. Liu, J. Appl. Phys. 62, 3866(1987).

65. R. J. Parker, Advances in Permannent Magnetism (Wiley, New York, 1990), p. 21.